

# The 2024 May event in the context of auroral activity over the past 375 yr

Mike Lockwood<sup>1</sup>  <sup>1</sup>★, Mathew J. Owens<sup>1</sup> , William Brown<sup>2</sup> and Manuel Vázquez<sup>3,4</sup>

<sup>1</sup>Department of Meteorology, University of Reading, Whiteknights Campus, Earley Gate, Reading, Berkshire RG6 6ET, UK

<sup>2</sup>British Geological Survey, The Lyell Centre, Research Avenue South, Edinburgh EH14 4AS, UK

<sup>3</sup>Instituto de Astrofísica de Canarias, Vía Láctea, E-38205 La Laguna, Spain

<sup>4</sup>Departamento de Astrofísica, Universidad de La Laguna, Vía Láctea, E-38205 La Laguna, Spain

Accepted 2025 May 17. Received 2025 May 17; in original form 2024 September 25

## ABSTRACT

We survey 223 916 auroral records from the Northern hemisphere observed between 1650 January and 2024 July, making full allowance for the secular change in the geomagnetic field. We generate criteria for defining extreme auroral events that are met on 0.015 per cent and 0.023 per cent of nights since 1650 and 1790, respectively. After discussing biases and trends in the data, we compare the event of 2024 May 10–11 with other extreme events and investigate the connections to geomagnetic and sunspot activity. Ranking the events by the lowest geomagnetic latitude from which aurora was observed, the second night of the 2024 May event is shown to be the third most extensive known, the most extensive being 1872 February 4. Allowing for dark adaptation of human vision, we find no evidence that this ranking has been greatly influenced by the increased use of modern digital cameras. We show that the area of the sunspot group from where the causal coronal mass ejection arises (identified by the associated flare) is weakly anticorrelated with the auroral and geomagnetic response; the scatter being large such that, although the 1872 February event arose from a rather small sunspot group, the 2024 May event arose from a large group, as did the ‘Carrington Events’ of 1859 August/September (ranked 2, 4, and 5). We show that the extreme events all occur during Carrington rotations for which the average open solar flux,  $F_S$  exceeds  $4 \times 10^{14}$  Wb but only 3.6 per cent of Carrington rotations when  $F_S$  exceeds this value give an extreme event at Earth.

**Key words:** solar–terrestrial relations–planets and satellites: aurorae–planets and satellites: magnetic fields–Earth–Sunspots.

## 1 INTRODUCTION

Aurora is caused by charged particles precipitating into the upper atmosphere. These may have originated in the solar wind by flowing along open field lines into the magnetosphere (Onsager & Lockwood 1997), but many will have moved up field lines from the ionosphere, where they were generated by the photoionizing extreme ultraviolet and X-ray radiations from the Sun (Welling et al. 2015). The balance between these plasma sources varies with the solar–terrestrial activity level. From the charge-state of ions in the inner plasma sheet region of the magnetosphere, the source region of auroral electrons before they are accelerated towards Earth (Kletzing et al. 2003; Sergeev et al. 2020), we know that in quiet times the solar source dominates but in times of disturbed space weather it is the ionospheric source that dominates (Kistler 2020). These charged particles are energized in the magnetosphere by the release of energy that had been extracted from the solar wind and stored in the geomagnetic field in the tail of the magnetosphere. The auroral particles precipitate down field lines and stimulate the emission of auroral light by atoms and molecules in the upper atmosphere.

The bands of latitudes around the geomagnetic poles where aurora most frequently occurs are called the *auroral ovals*. This term has

meaning at an instant of time, as well as statistically, because the aurora usually forms complete and continuous rings around the magnetic poles. During periods of high solar wind activity, when the power extracted from the solar wind is very high, the aurora grows in intensity and the ovals expand in both width and radius, bringing aurora to lower latitudes. These events are accompanied by large disturbances to Earth’s magnetic field that are called *geomagnetic storms*.

The nights of 2024 May 10 and 11 are among the latest examples of great auroral and geomagnetic storms, in which aurora is seen at exceptionally low latitudes. Such events have been the focus of a great many academic studies over many years (e.g. McNish 1941; Carapiperis 1956; Abbott & Chapman 1959; Livesey 1984, 2000; Allen et al. 1989; Silverman 1995, 2006, 2008; Silverman & Cliver 2001; Green & Boardsen 2006; Vázquez & Vaquero 2010; Hayakawa et al. 2016, 2018a, b, 2023c; Love & Coisson 2016; Kubota et al. 2017; González-Esparza & Cuevas-Cardona 2018; Boteler 2019; Hapgood 2019; Valach et al. 2019; Love, Hayakawa & Cliver 2019a; Berrilli & Giovannelli 2022; Hayakawa, Ebihara & Hata 2023a; Vichare et al. 2024). Some of these papers focus on the societal effects of the storms, others on the morphology and temporal development of the storm, while a third set analyses the causal solar wind disturbance. The causes and effects of the 2024 May event have recently been reviewed in detail by Hayakawa et al. (2025) and citizen science reports on the event have been used to study the

\* E-mail: [m.lockwood@reading.ac.uk](mailto:m.lockwood@reading.ac.uk)

auroral morphology by Grandin et al. (2024). Between 2024 May 2 and 9, a sunspot group traversing quite close to the centre of the solar disc (designated the identification number 13664 by the NOAA scheme) grew rapidly in total whole-spot area (the integrated area of all sunspot umbrae and penumbrae in the group) from 113 to 2761  $\mu$ sh (where 1  $\mu$ sh is a millionth of a solar hemisphere). Before it had rotated off the solar disc, this region had generated 14 ‘X-class’ flares and released 19 large coronal mass ejections (CMEs) with longitudinal width exceeding  $14^\circ$ , 10 of which were Earth-directed ‘halo’ events. The combined effect of these CMEs hitting Earth’s magnetosphere generated aurora at low and middle latitudes all round the globe. (Note that flare class classifications given here are as quoted in the literature cited but need adjustment based on the recent recalibration derived by Machol et al. 2022) (e.g. Hudson et al. 2024).

Knipp et al. (2021) have put such extremely large space-weather events into context using a ‘timeline’ representation. These authors also make the point that ground-based auroral observations have been a rather imprecise way of studying storms in the past. The reason is the large number of complicating factors that determine if an aurora is recorded, even if it is present at a given location. Perhaps the most obvious vagary is cloud cover: very intense aurora can be detected if cloud cover is thin or broken, but many displays are hidden from view by cloud. Secondly, there is the timing of the peak of the storm. The lowest latitudes of the aurora are around local magnetic midnight [i.e. the magnetic local time (MLT) is around 0 h] (Grandin et al. 2024) and so the Universal Time (UTC) of the storm alters the longitude at which the lowest latitudes will occur. This modulates the occurrence of reports, even from cloud-free locations, because of the geographical distribution of potential observers. A key factor in this is the distribution of human populations and reports are more common where population density is high, but with the complication that light pollution by street lighting in cities reduces the potential to see an aurora. However, the presence of humans is not sufficient: a fraction of those humans must be interested enough and able to observe, accurately record, and disseminate their observation.

During storms, some aurora is seen that is similar to that seen in the quiet or moderately disturbed periods, but is more intense and at lower latitudes. Visually, this aurora is either green in colour (the 557.7 nm atomic oxygen line arising from a transition from the  $^1S$  to the  $^1D$  electronic state) or with red above the green (the red being the 630 nm atomic oxygen line arising from the transition from the  $^1D$  to the ground,  $^3P$ , state). These auroras mainly originate from precipitating electrons of energies ranging from 100 eV to 100 keV (Rees 1969). The red is not seen for the more energetic electrons because they precipitate to lower altitudes in the upper atmosphere (to of order 100–120 km) where the long lifetime of the  $^1D$  state (110 s on average) means that the de-excitation is usually by collision rather than photon emission: the red line is *collisionally quenched*, whereas the green line is not because of the shorter (0.8 s) average lifetime of the  $^1S$  excited state. However, the electrons at the lower end of the energy range only precipitate to greater altitudes (from about 150 km to a maximum near 600 km) where they have enough energy to excite the  $^1D$  state but not the  $^1S$  state: at these altitudes the number densities of neutral atoms and molecules, and hence collision frequencies, are sufficiently low that the long-lifetime  $^1D$  state can de-excite by emitting a red photon. In addition, nitrogen molecules and molecular nitrogen ions in the upper atmosphere can generate blue and purple emissions, the dominant being a blue emission at 428 nm. These molecular nitrogen emissions are usually at low altitudes, but at high altitudes that are partially illuminated by sunlight, nitrogen can be

further excited by photons from the Sun giving a blue or mauve colouration at the top of arcs.

There is a second class of red aurora that appears during storms at lower latitudes. These last for several hours and usually occur when a sequence of magnetospheric substorms is in progress during a storm (Tinsley et al. 1986; Miyaoka et al. 1990; Rassoul, Rohrbaugh & Tinsley 1992; Shiokawa et al. 1994). These photons are red or blue/purple in colour. The red is the 630 nm line of atomic oxygen discussed above, the blue and purple is from vibrationally excited molecular nitrogen (Tinsley et al. 1984). A notable feature of these auroras is a very high red-to-green intensity emission ratio from atomic oxygen (Mikhalev 2024). Later, during the recovery phase of the storm, monochromatic red-line stable auroral red (SAR) arcs form at these lower latitudes (Kozyra, Nagy & Slater 1997). SAR arcs are thought to be generated by downward heat conduction carried by low-energy ( $< 10$  eV) electron precipitation that is produced when high-energy ring-current particles interact with the low-energy denser plasma in the plasmasphere. The outer plasmasphere is emptied during the initial phase of the storm as enhanced magnetospheric convection carries a plume of plasmaspheric material to the dayside magnetopause where it is lost to the magnetosheath when the field lines are opened by magnetic reconnection in the magnetopause (Zhang et al. 2018). After they have been re-closed by reconnection in the geomagnetic tail, these flux tubes are then refilled from the top-down by plasma upflow from the ionosphere below as they convect back along the dawn and dusk segments of the auroral oval to the dayside where ionospheric plasma densities are higher: this refilling takes place in quiet periods after the storm (Denton & Borovsky 2014). The red auroras seen during the initial main phase of the storm appear to be caused by a somewhat similar mechanism to SAR arcs, but their onsets are because of a very large storm-time increase in ring current ion fluxes that interact with the depleting plasmasphere in the mid-night sector (Shiokawa et al. 2013). This being the case, the migration of these red aurora to very low-latitudes during storms occurs because of the Earthward intrusion of the ring current at mid-night (Kataoka et al. 2024b), as seen in Energetic Neutral Atom imaging of the ring current during storms (Shiokawa et al. 2013). Note that the precipitating electrons that excite these low-latitude red auroras are of ionospheric, and not solar wind, origin.

Comparing modern events, such as the 2024 May storm, with historic observations is difficult (Grandin et al. 2024; Hayakawa et al. 2025). The human population has increased in numbers and spread into some areas of the globe that were previously only sparsely inhabited. In addition, modern cameras and ‘smart’ mobile phones, which, unless care is taken to fully attune to dark conditions, are more sensitive than the human eye, have provided observers with better means to record the phenomenon. Thirdly, social media, dedicated space weather internet sites, and citizen science projects such as *AuroraReach*, *Skywarden*, and *Aurorasaurus* give an easier and ready means to disseminate an observation. Lastly, improved forecasting now gives potential observers warning of probable events.

Since we submitted this paper, a very interesting paper by Love et al. (2025) has been published, which has similar aims of a comparative study of the lowest-latitude aurora during extreme events. However, there are differences between the two studies in that Love et al. (2025) look at the lowest geomagnetic latitude of discrete overhead aurora in specific events, whereas we survey all observations since 1650 but using the geomagnetic latitude of the observer to avoid discarding observations that were not known to be an overhead coronal form (and also avoiding the need to assume an emission altitude).

## 2 COMPARISON OF THE HUMAN EYE AND MODERN DIGITAL CAMERAS

Comparing the performance of the human eye and modern cameras in auroral observation is challenging due to fundamental differences in image processing and adaptation to light levels. The human eye, with its built-in neural processing, continuously adjusts sensitivity based on ambient light. Digital cameras, on the other hand, although increasingly sophisticated (particularly on smartphones) rely on sensor-based detection and algorithmic processing, rather than the complex neural adaptation and perceptual filtering performed by the human visual system. Other digital cameras use fixed sensor settings implemented by the operator. In this comparison, it is vital to remember that the absolute sensitivity of the eye increases by at least four orders of magnitude as it adapts to low-light conditions, but this process is slow and can take up to 2 h (Holmes 2016).

Photographers use *ISO sensitivity*, which is inversely proportional to the lower limit of detectable light intensity (Peterson 2016). A rough estimate often used by astronomers suggests that, for fully dark-adapted eyes, the equivalent camera ISO sensitivity usually ranges between about 800 and 2400, depending on the observer. However, this varies, even for the same individual and values up to 15 000 have been estimated for ideal observers in ideal conditions. In comparison, modern smartphone cameras automatically adjust ISO sensitivity between 100 and 1600, while advanced cameras can reach significantly higher values. Excessive ISO values, however, introduce noise into camera images, which can degrade quality.

These rough estimates suggest that the human eye can outperform a digital smartphone camera, provided it has been fully attuned to dark conditions. Because of the importance of this to the comparison of the 2024 May auroral event (in which many observations were made using smartphones) with previous events (when smartphone cameras were not available), this section explores the eye-camera sensitivity comparison in greater detail.

Experiments indicate that the low-intensity limit of detectability for top-quality digital cameras and fully dark-adapted human eyes are comparable (e.g. Vasil'ev & Tibilov 2018). None the less, auroras are quite often reported as visible to a camera but not to the naked eye. This will often occur because the observer's eyes have been exposed to some stray light in the preceding one or two hours, preventing full dark adaptation (Holmes 2016). The properties of dark adaptation have been established since the early 20th century, with classic studies such as Aubert (1864) and Hecht (1920), later added to and summarized by, for example, Pirenne (1962), Graham et al. (1965), Tredici & Miller (1985), and Kalloniatis & Luu (2007). It should also be noted that the time taken for an eye to adapt to the dark increases with the brightness of the light the eye has previously been exposed to (Graham et al. 1965). All these experiments show that the threshold luminance for an average human eye is approximately  $0.25 \text{ cd m}^{-2}$  in daylight.

Luminance is the intensity of light emitted from a surface per unit area in a given direction and its SI units are  $\text{cd m}^{-2}$ , sometimes called a 'nit'. Because it is the intensity emitted in a set direction (per unit solid angle), for scatter-free propagation it does not depend on the distance between the source and detector. Older studies often use the non-SI unit of Lamberts ( $L$ ) for luminance where  $1L = (10^4/\pi) \text{ cd m}^{-2}$ . Upon entering complete darkness, 'scotopic vision' sets in after about 8 min, by when the threshold luminance for the average eye is reduced to about  $10^{-2} \text{ cd m}^{-2}$ . Over the next 30 min, the threshold luminance for the average eye continues

to decay exponentially, asymptotically approaching a limit near  $3 \times 10^{-5} \text{ cd m}^{-2}$  (Graham et al. 1965; Tredici & Miller 1985; Kalloniatis & Luu 2007). However, due to individual variability, this limit can be either larger or smaller by a factor of 3. Under ideal conditions, the rods in the human eye can detect single photons (Holmes 2016). To minimize noise, visual signals are pooled by bipolar and ganglion cells before transmission to the brain via the optic nerve, a process called 'convergence'. The brain integrates these signals over approximately 10 ms. This was first analysed by Hecht, Shlaer & Pirenne (1942) and the convergence ratios later refined by Dey et al. (2021). Analysis of these numbers also yields a threshold luminance of order  $10^{-5} \text{ cd m}^{-2}$ , which is what is found by experiment for the most sensitive eyes and what we here term as the 'ideal limit' (Dimitrov et al. 2008). In practical situations, as opposed to laboratory experiments, additional factors such as observer age, retinal noise, and eye movement may elevate the effective threshold luminance from the ideal  $10^{-5} \text{ cd m}^{-2}$  to a value closer to  $10^{-4} \text{ cd m}^{-2}$ .

Additionally, scotopic vision does not involve colour-detecting cone cells, and the threshold luminance depends on wavelength. The experiments show that the ideal limit for white light is  $10^{-5} \text{ cd m}^{-2}$ , but for specific auroral emissions, it differs: for the atomic oxygen red line (630.0 nm), it is around  $7 \times 10^{-3} \text{ cd m}^{-2}$ , for the atomic oxygen green line (557.7 nm) it is near  $10^{-5} \text{ cd m}^{-2}$ , and for molecular nitrogen ion violet emissions (427.8 nm), about  $2 \times 10^{-6} \text{ cd m}^{-2}$  (Chapanis 1947; Graham et al. 1965; Kalloniatis & Luu 2007). These are also ideal limits that, like that for white light, may be greater by an order of magnitude in practical situations. Because scotopic vision is mediated by rod cells rather than cone cells, auroras can appear white to human observers (sometimes called the 'Purkyně effect'), whereas cameras will always distinguish the different emission wavelengths.

To compare this with camera performance on minimum detectable luminance, we use the equation from Thomson (2005):

$$L_a = \frac{15.4N^2}{E_i \times t}, \quad (1)$$

where  $N$  is the relative aperture (stop number), defined as  $N = f/D$ , where  $f$  is the focal length and  $D$  is the aperture diameter.  $E_i$  is the exposure index (equal to ISO for automatic cameras such as on smartphones), and  $t$  is the integration time. For an iPhone 13, for example,  $f = 26 \text{ mm}$ ,  $D = 16.25 \text{ mm}$ , giving  $N = 1.6$ , and using the maximum iPhone ISO value of 7600 and maximum integration time of  $t = 0.33 \text{ s}$ , we obtain a luminance threshold of  $L_a = 1.6 \times 10^{-2} \text{ cd m}^{-2}$ . Unlike the human eye, this value is nearly constant across wavelengths.

Thus, the iPhone 13 is significantly less sensitive than a well-attuned human eye, which may detect luminance levels as low as  $10^{-5} \text{ cd m}^{-2}$ . The well-attuned human eye is therefore up to about 1600 times more sensitive under ideal conditions. Even if we raise the threshold from the ideal limit by a factor of 10 the well-attuned eye is still more sensitive than a smartphone camera by a factor of 160. However, for an observer with no dark adaptation ( $L_a \approx 0.25 \text{ cd m}^{-2}$ ), the iPhone 13 is about 6.5 times more sensitive.

Other digital cameras can achieve lower  $L_a$  values. A Micro Four Thirds (MFT) camera with an integration time of  $t = 30 \text{ s}$  yields  $L_a \approx 10^{-2} \text{ cd m}^{-2}$ , making it also more sensitive than an unadapted eye but less sensitive than a fully dark-adapted eye. However, a top-tier professional DSLR camera with  $t = 30 \text{ s}$  can achieve  $L_a$  between  $10^{-4}$  and  $10^{-5} \text{ cd m}^{-2}$ , making its sensitivity comparable to that of the dark-adapted eye. These values are summarized in Table 1.

**Table 1.** Comparison of luminance thresholds for some different imaging systems. The human eye is considered when fully attuned to dark conditions and the iPhone 13 is considered for maximum automatic adjustment to dark conditions.

Device	Minimum luminance $L_a$ (cd m <sup>-2</sup> )	Integration time $t$ (s)
Human eye (ideal)	$10^{-5}$	0.01
Human eye (violet, ideal)	$2 \times 10^{-5}$	0.01
Human eye (green, ideal)	$3 \times 10^{-5}$	0.01
Human eye (red, ideal)	$7 \times 10^{-4}$	0.01
Human eye (practical)	$10^{-4}$	0.01
iPhone 13	$1.6 \times 10^{-2}$	0.33
MFT Camera	$10^{-2}$	30
Professional DSLR	$10^{-4}$	30

Thus, while cameras surpass the unaided human eye that is not properly attuned to dark conditions, the fully dark-adapted human eye remains highly competitive with even top-tier digital cameras. This contradicts the frequently made assumption that digital cameras (and in particular smartphone cameras) always outperform human vision and highlights the remarkable dynamic range and adaptability of the human eye-brain system. Considering colours, the eye is most sensitive at the violet end of the visible spectrum and least at the red end. Even allowing for a factor of 10 increase in threshold luminosity over the ideal limit, the fully dark-attuned eye still performs better than an iPhone camera for the auroral red line wavelength and is only marginally less sensitive than a DSLR digital camera. However, because of the lack of contribution by cones in the eye, the Purkyně effect means that the observer may well see very faint red aurora as white and so class it as either green aurora or, potentially, as light pollution.

These considerations have a crucial implication. The comparison between naked-eye and camera observations is meaningless unless the precautions taken to attune the human eye are known and documented. There are many examples in the literature and on social media that describe aurora that was invisible to the naked eye, yet were seen by digital camera (e.g. Shiohara, Ogawa & Kamide 2005; Kataoka et al. 2024b; Vichare et al. 2024). The voracity of these reports is not in question; but one must be very careful about how this information is used. These examples in no way prove that this is always the case. If the naked eye in question was not fully attuned to dark conditions (and this would include lack of dark adaptation caused by looking at digital camera or computer screens prior to observation), then this is entirely what we should expect. However, if the eye were fully dark-adapted (for a human with good vision) then the sensitivity of the camera and the naked eye could be broadly similar. For almost all reports, historic and modern, we have little or no information about the ambient light levels in the immediate vicinity of the observer, nor about how long the observer was in such conditions prior to observing an aurora. We cannot speculate on either point. Hence, we have no scientific option but to allow for the possibilities that the naked eye may or may not be as sensitive as a camera. We know of no cases for which camera observations were reported, and naked eye observations were reported to not be possible, even though all precautions were taken to make the eyes fully dark-attuned (i.e. that the observer had spent at least an hour in dark conditions and had not in that time looked at a digital camera or computer screen). We also note that, just as the eye is not a standard instrument in terms of its sensitivity, nor is the camera: the ISO factor can vary a great deal with the camera quality and design, and

for cameras with automatic ISO selection (such as on smart phones) this will also vary automatically with the light level.

In this paper, we only compare events by the lowest geomagnetic latitude at which the aurora was observed. There is a selection effect inherent in this. For a given event, the lowest latitude (absolute value) where aurora was observed with the naked eye would tend to be where the best conditions for the observer were present and that means having the most well-attuned eyes as well as other factors (such as atmospheric conditions, light pollution, and the intensity of the auroral light). All other factors being equal, the lowest-latitude, naked-eye observation will be by the observer who has attuned his/her eyes best to the darkness. Hence, there will be a tendency for the lowest latitude naked-eye observation to be made by an observer with well-attuned eyes. (Note this a tendency and certainly not a requirement). As discussed above, the sensitivity of such an observer could be at least as high as that of a smartphone and will rival that of a higher grade digital camera.

The advances in cameras, event forecasting, and event reporting have only improved recording of aurora over approximately the last 20 yr when the number of potential observers was greatly increased by individuals with cameras on their smartphones. Before that, records came from the diaries of scientists and enthusiasts, log books generated by observatories, expeditions, and commercial ships, meteorological reports, and newspaper reports. There are other, unexpected, sources. For example, because a bombing raid on London during the 1914–1918 war had been facilitated by the illumination of the River Thames by aurora (navigation techniques at night were minimal at the time), the British Air Ministry thereafter collected auroral sightings and many were provided by the many lighthouse keepers around the coasts of Britain (Lockwood & Barnard 2015). Logbooks of ships at sea are a small but valuable resource because they help to fill in some of the gaps between centres of population. However, all of these sources of information on the aurora were in decline from about 1950 onwards and before the internet became a factor, auroral reporting was at a lower level than at any time since the 18th century. Reports in newspapers and the literature have become restricted to major events, and newspapers often now carry more forecasts of auroral events than after-the-fact reports on them.

These factors mean that it is not straightforward to compare the 2024 May event to past events. In this paper, we present a method that is designed to try to minimize the effect of the changes and put the 2024 May event in context with other great storms. This is important because in all reconstruction work we aim to make the historic data set as homogeneous as possible so that we can extrapolate data taken during the space age back to earlier times, as has been done for both continuous data series (e.g. Lockwood et al. 2022a, b) and for extreme events (Owens et al. 2021; Cliver et al. 2022a).

The key point for the logic of this paper is that it cannot be assumed that the camera is always more sensitive than the eye. Hayakawa et al. (2025), for example, make this a key assumption of their analysis but this section shows that we cannot make that assumption. The relative sensitivity of a modern digital camera and the human eye depends on the level to which the eye is adapted to the dark, which is almost always unknown, and on the colour of the aurora, which is often unknown and is very likely to be incorrectly recorded by naked-eye. In historic observations, we almost never know the level of dark attuning of the observer's eyes and we cannot make guesses about what it might have been. Hence, camera-eye distinctions are effectively meaningless because we do not have enough information to make them in almost all cases.



### 3 METHODS

This paper studies auroral observations in the interval 1650 January to 2024 July to place the major, global auroral event of 2024 May 10–11 in context. Because of the complications discussed in Section 2, we need to formulate a method to process auroral observation data.

#### 3.1 Processing of auroral samples

This paper combines several catalogues of auroral observations. These include early ones by Frobesius (1739), Mairan (1754), Boué (1856), Wolf (1857), Lovering (1868, and subsequent papers in the series), Fritz (1873), Seydl (1954), Angot (1896), and Křivský & Pejml K. (1999). To these were added the later extensive collections of Sam Silverman that covered the USA, Canada, and Greenland (now held by the National Space Science Data Centre, NASA Goddard Space Flight Center) (Silverman 1992, 1995, 1998, 2006, 2008). Also included are observations found in searches by the authors Manuel Vázquez (Europe) and Mike Lockwood (UK) (some of which were used in the papers by Vázquez et al. 2016 and Lockwood & Barnard 2015, respectively). In addition, we have added verifiable observations reported in the literature, newspapers, and on the internet to bring the collection up to July 2024. The dominant sources of observations since about 2010 have been the image gallery of the Spaceweather.com website, the Skywarden and Aurorasaurus citizen science projects, and the results of internet searches of websites such as AuroraReach, of newspapers and observatories, and posts on a variety of dedicated aurora-watching Facebook groups. The relatively small numbers of records available from academic papers have also been added. In all cases, the relevant image or images were inspected and cases that were not clearly aurora or of dubious provenance were rejected. Of the 1611 reports of aurora during the storm of 2024 May 10 and 11, the largest contribution of was from the auroral image gallery of Spaceweather.com, followed by the collection by Grandin et al. (2024), obtained using an online survey, supplemented by sightings reported via the Skywarden project. These provided, respectively, 690 and 519 reports, and the remainder came for internet searches of newspaper and social media sites and academic papers.

Given that we want the data base to be as homogeneous as possible, we have to be aware of the effects of changes in human population (number and distribution), their behaviour and the technologies available to them. Modern observations are recorded on the internet via image contributions to space weather sites and social media, and via citizen science activities. That these reports usually give an image of the sighting is useful as one has a chance to identify and discount glows that are light pollution, airglow, sprites, elves, blue-jets, haloes, or nacreous clouds. Light pollution has become a particular problem in recent years because a mixture of blue and red LED lamps are increasingly used in greenhouses to help the tomatoes and strawberries grow and ripen and at sports stadia to help the pitch grass grow. These generate a pink glow in the atmosphere, particularly if cloud is present, which is often mistaken for aurora.

The images are generally recorded on smartphones or using higher resolution and higher sensitivity cameras. As discussed in Section 2, these can have considerably greater sensitivity than the un-attuned human eye, so low-intensity aurora can now be recorded that may not have been noted by visual observers in the past. However, the difference between cameras and the eye depends on wavelength, and so auroras of different colours are differently affected and observers who have not given their eyes enough time to adjust to dark conditions (up to 2 h) will not see aurora that can be detected by camera.

Observers now often go searching for aurora based on reasonably accurate forecasts and use their cameras to find it. Note that doing so takes the observer out of scotopic vision and hence subsequently they will tend not to see the aurora by naked eye. We note that one image of aurora on 2024 May 10/11 from the Big Island, Hawaii arose because the observer was photographing meteors and only later realized that there was a backdrop of auroral light that his camera had detected where his eyes had not. However, in this particular case, other accounts from the Big Island that night are specific in saying the observer saw the aurora visually before taking the photograph: for example, Brenda Trowbridge of Naalehu, Hawaii is quoted in the Kaua'i News Hawaiian newspaper as spotting the aurora without her camera, before fetching it to take photographs. The important issue of comparing modern day, camera-assisted, and internet-reported observations with past naked-eye observations is discussed below in Section 4.7.

To help maintain some consistency with historic observations, we do not use any long exposure images (in which stars are extended into lines) nor images taken from aircraft. Unfortunately, fakes are a childish yet growing problem with internet records. At present, an experienced observer can readily identify artificial intelligence (AI)-generated and heavily photoshopped auroral images; however, that might change in the near future as AI becomes more sophisticated. More difficult to identify are genuine images of past auroral events posted with fake location and/or time labels – an internet phenomenon we term ‘image recycling’. Usually the images chosen for this are the most striking ones, and internet image searches provide a way of checking the true provenance. In addition, recycled images of dramatic multiple green arcs, characteristic of high latitude aurora, are often attributed to low latitude sites where a diffuse red glow is expected. Because of these faked reports and because of genuine mistakes caused by airglow and greenhouse light pollution, we adopt a ‘precautionary approach’, whereby a report over which there is any doubt is rejected. This undoubtedly leads to genuine reports being omitted, but there are other factors that cause aurora to go unreported, such as clouds or the lack of the right person (with dark-adapted eyes) being in the right place at the right time and observing the sky. In the current survey, about 900 observations were rejected after such checks. The number of individuals perpetrating fakes is fortunately small, and the (online) names of culprits can help identify suspect images. For modern data, we do not use observations that are more than  $10^\circ$  equatorward in magnetic latitude than any other observation on that night (or the previous or next night) and this removes many of the observations suspected of being spurious. Area-combined samples (see below), based on only one observation, are particularly scrutinized and rejected if their magnetic latitude is below the  $2\sigma$  point of the overall distribution, unless it is from a trusted source (such as an observatory or a known researcher in the field) and/or corroborated by one or more independent report.

Another great change is the population of humans and their distribution. The important element of the population are the individuals that have the interest to make an observation, often travelling as tourists to latitudes where aurora is common, and the means to record and report them. Hence, population growth, education, auroral tourism, cameras, better forecasting, and the internet have all acted to increase the number of recorded auroral sightings in the past three decades. Unfortunately, this rise came after a fall when newspapers took less interest and specialist laboratories closed or turned their attention to other phenomena.

We use only Northern-hemisphere observations in order to maintain a degree of consistency over the past 400 yr. Observations from the Southern hemisphere are rarer because a much larger fraction

of that hemisphere at auroral latitudes that is covered by oceans, and recorded observations at sea are much rarer than from on land. However, using data from only one hemisphere has the disadvantage of introducing an annual modulation into the data due to the tilt of the Earth's rotational axis with respect to the ecliptic and the fact that aurora is usually very hard to detect in sunlight. In summer, this makes aurora almost completely undetectable at high geographic latitudes and reduces the hours in a day during which it can be seen from middle latitudes. Were observations as common from the Southern as the Northern hemisphere, this annual variation could be eliminated by using data from both hemispheres. However, that is not the case, and so we would have an annual modulation of the data even if we included Southern hemisphere observations. Aurora is ordered by geomagnetic latitude, which varies with geographic latitude and longitude (due to the offset of the geomagnetic and rotational axes) and with date because the secular variation in Earth's magnetic field causes changes to the relative orientation of those two axes.

There are further complications. Earth's magnetic axis is not geocentric and its eccentricity causes Universal Time (UT) variations in solar wind-magnetosphere coupling (Lockwood et al. 2021; Lockwood & Milan 2023) and this means that the arrival time of an interplanetary disturbance alters the effect that it has and there are longitudinal differences in the response (Lockwood, Owens & Barnard 2023).

Although explicit duplications of observations have been removed, many remain. This is inevitable as catalogues of auroral recordings often contain records of an auroral observation that are carried forward from a prior catalogue (often without giving the provenance) and site names or the location coordinates have been updated and/or slightly adjusted. This means that combining catalogues can cause duplicated records that are not always recognized as such. In addition, when surveying historic newspaper reports, the same observation is often reported differently by different newspapers. In some cases, the duplication leads to errors and checking original sources is a very important and ongoing activity (e.g. Hayakawa et al. 2016). To avoid undue weight being given to multiple records to what may have been a single observation of aurora, we here use a new approach. Records on a given night that are within  $0.2^\circ$  of each other along the great-circle path (about 22 km in distance) are here treated as just one independent sample that is given the mean latitude and longitude of the combined reports. The angular separation of  $0.2^\circ$  was chosen after a sensitivity study of the balance between the number of observations that are combined and the loss of spatial resolution. This process yields 195 233 independent area-combined samples from the total of 223 916 reports on 136 966 nights (an average of 1.63 per night). There are 48 975 nights on which at least one report was made: this means that aurora was seen, at some location, on 35.76 per cent of all nights. Note that the total number of area-combined samples is only 12.8 per cent smaller than the number of observation reports. A large factor in this is that samples from rural areas often result from a single reported observation, but some samples from major centres of population (without strong street lighting) can result from recordings from several tens of observers. Although multiple observers give greater credence to the observation, without this process the geographical distribution of population (specifically, the population able and willing to record their observation) would even more strongly modulate the statistics of auroral occurrence and in a way that changes with time.

In general, neither the colour nor the position in the sky is considered here because it is a relatively small subset of historic observations that give this information. Grandin et al. (2024) have studied citizen science reports from the 2024 May event and find

the distributions in magnetic latitude of reports of predominantly green and predominantly red aurora were very similar at geomagnetic latitudes above  $47^\circ$  but the colour red dominated below this latitude. On this, we note the difference in colour perception for camera and eye observations and Hayakawa et al. (2025) do not find such a clear latitudinal distinction. The nature of the observation site identifier given varies widely. In a very small number of cases it is coordinates (computed with varying degrees of accuracy); in other cases, it is a specific building or monument that can be pinpointed to a few tens of metres; others give the name of a small village or town or a district within a city. However, many just give the name of the town, city, or state or even just the country. The distance from an observer who sees a full coronal (overhead) auroral form to a second observer who can see the same portion of aurora-lit sky at an elevation of at least  $20^\circ$  above the horizon is, respectively, 230, 310, and 690 km for emission altitudes of 90 km (roughly the base of the oxygen green line emission), 120 km (roughly the top of the green line emission), and 300 km (typical emission height for the oxygen red line). These distances correspond to roughly  $2.1^\circ$ ,  $2.7^\circ$ , and  $6.2^\circ$  in great circle distance. Given the colour is often not recorded, we have to assume an altitude and the lowest altitude gives that the same patch of auroral sky is visible over a circle of diameter of order 460 km. To put this in context, we note that London, for example, has an east–west diameter of 58 km and a north–south diameter of 40 km and hence giving the coordinates of the centre of London for any observation described as from ‘London’ is within allowable uncertainties. On the other hand, the country of England has dimensions of about 330 km east–west and 570 km north–south, and hence using the centre location of a sighting labelled as ‘England’ would not cover all locations in England to within an acceptable error. Hence, the central location is acceptable for most major cities and smaller locations, but observations labelled by the name of the country or of a large county, state or region are usually not. Thus, we use the central location for a given definition of a location but only if all places that could be interpreted under that name are within about 50 km of that central location.

We use the astronomical definition of a ‘night’, which extends for 24 h from local mid-day. However, in many catalogues or reports of observations, no Universal (UT or UTC) nor local time is given, hence one cannot be sure the same definition has been used by the observer. As a result, every report date is here treated as having an uncertainty of  $\pm 1$  d because observations made after local mid-night may have been labelled with either date.

In this paper, we look only at the geomagnetic latitude of the observer. This is not the most physically meaningful parameter: we would really like to know the geomagnetic latitude of the precipitation causing the aurora that the observer detects. In particular, we would like to know the lowest geomagnetic latitude of that precipitation as a measure of the extent of the aurora and the magnitude of the event. Given enough information about the height of the auroral emission (which can sometimes be inferred from the colour, and the elevation range over which it is seen), we could compute the offset between the observer and the relevant field line and this has been done for modern observations. For example, Vichare et al. (2024) find this offset was greater than  $17^\circ$  for a well-documented and comprehensive set of recent observations from Hanle India in 2023 April of high-altitude red aurora. Allowing for the offset for historic data has been attempted, for example it was done by (Knipp et al. 2021) in the formulation of the ‘timeline’ event graphic and several other publications. The problem is that for historic sightings we usually do not have such good information and for many we have none at all: hence there is not only uncertainty in the

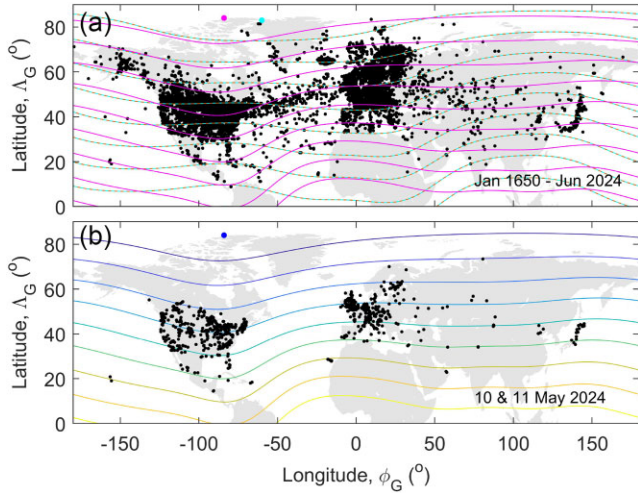


**Figure 1.** The global distribution of area-combined auroral observations (samples) used in this paper. Part **A** is for all of the 195 233 area-combined samples from the interval 1650 January to 2024 July. The mauve contours are QD geomagnetic latitudes (see Section 3.3),  $\Lambda_M$ , of  $[0:10^\circ:80^\circ]$  for 2024 and the brown and cyan dashed contours are the same for 1650. The mauve and cyan dots give the corresponding north magnetic pole locations for these years. Part **B** is for the 841 area-combined samples for the nights of 2024 May 10 and 11. The coloured contours (yellow to dark blue) are QD geomagnetic latitudes,  $\Lambda_M$ , of  $[0:10^\circ:80^\circ]$  for 2024 May and the blue dot is the north magnetic pole location.

offset for a given report, but also we cannot quantify that uncertainty for that observation. We here generate a data base of the geomagnetic latitudes of the observer and make no attempt to compute the latitude of the causal precipitation, thereby not introducing yet another difference between historic and recent observations.

Fig. 1 **A** shows a map of the locations of the area-combined observation samples used in this paper for the entire interval (1650 January to 2024 July). The map shows a dearth of observations from Siberia, compared to other areas on the Northern-hemisphere land mass and even compared to the North Atlantic, where shipping has provided regular sightings. This is largely a consequence of the low population density in this region. There are catalogues of Siberian auroral observations that have been constructed (e.g. Ptitsyna & Demina 2021), but these are not available online and some need translating from Russian. Future work will extend the survey to try to better fill this longitude gap. More samples have appeared in recent years as auroral tourism to Siberia has increased, but numbers are still low and the number of sites in Siberia from where aurora are recorded is still low. Social media posts from inhabitants tend to be in Russian and many internet posts are on commercial sites selling images that tend to give the locations of auroral images but not the date on which it was recorded. Part **B** of Fig. 1 shows the corresponding map for the 841 area-combined samples on 2024 May 10–11 in our data base. The contours are relevant quasi-dipole (QD) geomagnetic latitudes,  $\Lambda_M$  (see Section 3.3).

In the first hundred years of the survey (1650–1750), there are, on average, just 0.19 records per night (and aurora was observed at some location on just 8.18 per cent of nights). This figure initially rises with date and for 1750–1850 the average is 0.84 per night (with aurora seen on 28.26 per cent of nights) and for 1850–1950 it is 3.96 per night (with aurora seen on 63.62 per cent of nights). For the latest 74.5 yr (1950–2024 June) the average has fallen again to 1.21 samples per night (with aurora seen on 45.25 per cent of nights),

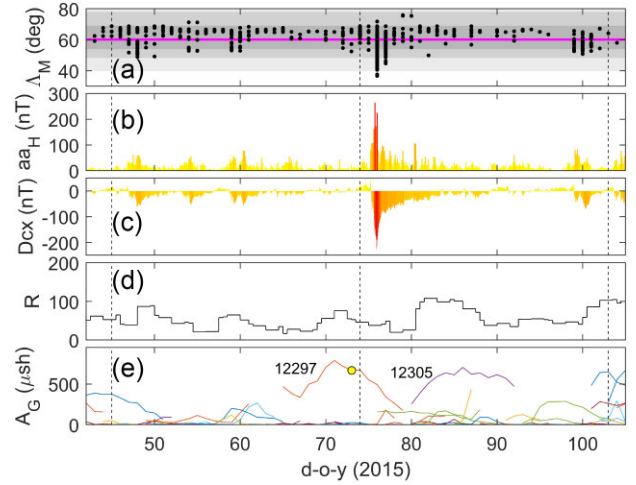


**Figure 2.** An example of geomagnetic and auroral storm, the ‘St. Patrick’s Day storm’ of 2015 March 16–18. **A** shows the QD geomagnetic latitude  $\Lambda_M$  of samples of area-combined auroral observations. The grey areas delineate values from  $\Lambda_M$  distribution for all the samples in this survey presented in this paper (1650 January–2024 July): the light-grey, mid-grey, and darker grey areas delineating values that are within, respectively, the  $\pm 3\sigma$ ,  $\pm 2\sigma$ , and  $\pm 1\sigma$  points of the distribution, the mean that is shown by the mauve line (see Section 4.3). **B** 3-hourly values of the homogeneous  $aa_H$  geomagnetic activity index (Lockwood et al. 2018a, b) in a bar-chart format where the vertical bars are coloured according to their height. **C** The same as **B** for hourly values of the  $Dcx$  geomagnetic index (Karinen & Musula 2005). **D** shows the International sunspot number  $R$ , and **E** the area (in millionths of a solar hemisphere,  $\mu sh$ ) of sunspot groups: the major groups are numbered using the NOAA identification scheme and the yellow dot marks an C9.1/1F-class solar flare that occurred in group 12297 and was associated with the launch of the CME that hit Earth causing the geomagnetic and auroral storm. The vertical dashed lines delineate the intervals used to generate the global precipitation maps in parts **A** and **B** of Fig. 5. Note that the horizontal axis is in fractional day-of-year, which is zero at 00:00 UTC on January 1.

and that has remained roughly constant (for example, for after the year 2000 the number is 1.25 (with aurora seen on 38.33 per cent of nights). Hence, during the 2024 May 10–11 the number of reports per night was higher than the recent average for the time by a factor of about 270.

### 3.2 An example of a well-studied storm in the data set

Fig. 2 is an example of the auroral records in a large (but not extreme) auroral event. This is the ‘St Patrick’s Day’ storm that occurred on 2015 March 17 and 18. The interplanetary causes of this storm and some of its effects have been studied by Wu et al. (2016) and by Jacobsen & Andalsvik (2016) and the consequent aurora was studied by Case & MacDonald (2015) from data collected by the *Aurorasaurus* citizen science project. The effect of this storm on the energetic electron population in the outer radiation belt has been studied by Pierrard & Lopez Rosson (2016), as will be discussed further in the next section. The black dots in Panel **A** of Fig. 2 show the QD geomagnetic latitudes  $\Lambda_M$  (see Section 3.3) of the area-combined auroral samples in intervals of durations 28 d before and after the main phase of this storm. The light-grey, mid-grey and darker-grey areas delineating  $\Lambda_M$  values that are within, respectively, the  $\pm 3\sigma$ ,  $\pm 2\sigma$ , and  $\pm 1\sigma$  points of the distribution for all area-combined samples in this survey (covering January 1650 to July 2024) and the mean is shown by the mauve line (see Section 4.3). Panel **B** shows the 3-hourly values of the homogeneous  $aa$  geomagnetic activity



index,  $aa_H$  (Lockwood et al. 2018a, b) in a bar-chart format, where the vertical bars are coloured according to their height. Panel C is the same as B, but for hourly values of the  $D_{cx}$  geomagnetic index.

Throughout the paper, we use the  $D_{cx}$  index in preference to  $Dst$ .  $D_{cx}$  was introduced by Karinen & Musula (2005) and has a number of advantages:  $D_{cx}$  extends back to 1932, whereas  $Dst$  only extends back to 1957;  $D_{cx}$  is also more homogeneous in its construction and uses better weighting of stations than  $Dst$  (Mursula, Holappa & Karinen 2011). Like  $Dst$ ,  $D_{cx}$  is increasingly negative for greater disturbance levels and is strongly modulated by the ring current in Earth's inner magnetosphere. (However, it is also influenced, to a lesser extent, by the currents that flow in the magnetopause boundary).

The sunspot group areas are retrieved from the [Debrecen Photoheliographic Database](#), maintained by the Heliophysical Observatory. The data have been processed as described by Baranyi, Györi & Ludmány (2016) and consistency with the earlier data from the Royal Greenwich Observatory (RGO), which are also available in the same data base, has been improved and recalibrated by the work of Györi, Ludmány & Baranyi (2017). There has been discussion about sunspot group area estimates because those from the USAF (United States Air Force) Solar Observing Optical Network are consistently lower than obtained from other data and by other methods by of order 25 per cent–50 per cent (Meadows 2020). However, the Debrecen areas agree well with other estimates (e.g. Mandal et al. 2020).

The storm is seen as a very prominent peak in  $aa_H$  and an equally clear minimum in  $D_{cx}$ . It can be seen that the aurora moves to just below the  $3\sigma$  magnetic latitude at the event peak, but most of the time before and after the storm, the aurora is almost always poleward of its mean location and equatorward of the upper  $1\sigma$  value of the overall  $\Lambda_M$  distribution. In this case, there is a clear location of solar origin with a dominant sunspot group (12297) near the centre of the solar disc that gave rise to a C9.1/1F-class flare (Bamba, Inoue & Hayashi 2019) that was associated with a CME that was observed using the LASCO (Large Angle and Spectrometric Coronagraph Experiment) coronagraph on the SoHO (Solar and Heliospheric Observatory) satellite early in its propagation to Earth and then detected in near-Earth space by the *Wind* spacecraft in orbit around the L1 Lagrange point (Wu et al. 2016).

Fig. 3 presents a composite of 13 images of the Northern-hemisphere aurora around local mid-night during the St Patrick's Day storm. These are measured by the VIIRS (Visible Infrared Imaging Radiometer Suite) instruments on the Suomi-NPP satellite at visible and near-infra-red wavelengths (500 to 900 nm) (Shao et al. 2016; Kalb et al. 2023). This band covers the primary emission lines of atomic oxygen (green at 557.7 nm and red at 630 nm) as well as the molecular nitrogen emission lines in the range 391.4 to 470.9 nm (blue and violet) that are observed in auroras. The images have been filtered and dynamically scaled using the 'ERF-dynamic scaling' procedure, which brings out bright features (without saturating the image) but tends to suppress broad diffuse regions. These images show that, although some ground-based observations of the aurora are within the oval, as imaged from space in this way, many of the ground-based observations, at all longitudes, appear in the region of considerably lower intensity, equatorward of the main oval. Note also that time development of the auroral emission aliases with the observation intervals, sometimes giving sharp boundaries between the images.

We have also generated the equivalent to Fig. 3 using image swaths observed on the same night by the Special Sensor Ultraviolet

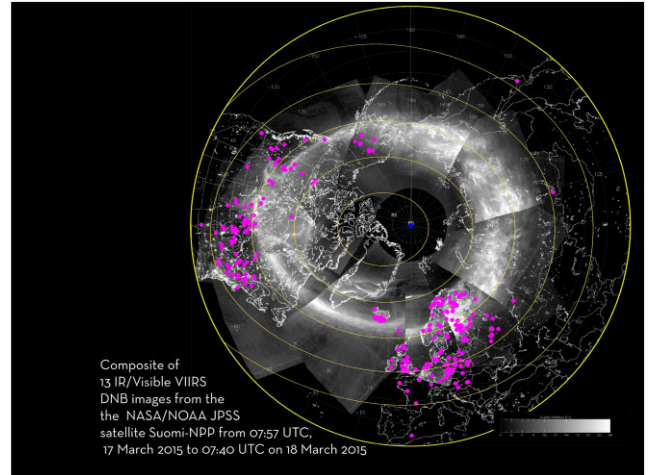


**Figure 3.** A composite of 13 DNB (Day/Night Band) Images from the VIIRS (Visible Infrared Imaging Radiometer Suite) instrument on the Suomi-NPP (Suomi National Polar-orbiting Partnership) satellite, a joint NOAA/NASA mission. These were recorded between 07:57 UT on 2015 March 17 and 07:40 UT on 2015 March 18 during the St. Patrick's Day storm and were filtered and scaled using the 'ERF-dynamic scaling' algorithm and provided by Curtis Seaman (<https://rammb.cira.colostate.edu/projects/npp/blog/index.php/uncategorized/the-aurora-seen-around-the-world/>). The mauve dots are locations from which aurora was reported from the ground on 2015 March 17 and 18 and the orange contours are QD geomagnetic latitudes,  $\Lambda_M$ , of  $[40^\circ:10^\circ:80^\circ]$  for the date in question. The yellow circle is at geographic latitude  $\Lambda_G = 35^\circ$  and the blue dot is the geographic pole ( $\Lambda_G = 90^\circ$ ). Auroral images are courtesy of the VIIRS Imagery and Visualization Team, CIRA, Colorado State University, USA.

Spectrographic Imager (SSUSI) far ultraviolet (FUV) imagers on the Defense Meteorological Satellite Program (DMSP) F18 satellite (not shown). The same feature of many ground-based observations being equatorward of the main oval seen from space is noted, but it is to a lesser extent than in Fig. 3: this is because the auroral oval seen in the FUV images reaches somewhat lower latitudes than is seen in the IR/Visible images. We note that Kosar et al. (2018) used DMSP-SSUSI data to compare the auroral oval boundaries at local mid-night during the St Patrick's Day storm, as derived from the ground-based and by DMSP/SSUSI observations. They found an agreement, but it was not a close agreement. There are a number of reasons why auroras can be seen on the ground when it is not seen from space. One is temporal variations, because the relevant part of the satellite image is not, in general, recorded at the same time as the ground-based observations. The second is intensity levels: broad diffuse emission regions tend to be lost in space-based images when filtering and image-processing is aimed at highlighting the bright discrete structures in the presence of a large dynamic range of emission intensity.

### 3.3 Choice of the definition of geomagnetic latitude

There are a number of geomagnetic latitude estimates used in studies of solar-terrestrial science, and there are differences between them. Each has its particular strengths and weaknesses in relation to a given application. These include dip latitude, apex latitude, modified apex latitude, invariant latitude, corrected geomagnetic latitude, PACE coordinate latitude, constant B-Minimum coordinate latitude; Altitude-Adjusted Corrected Geomagnetic latitude and QD latitude (Richmond 1995; Shepherd 2014; Laundal & Richmond 2017).



All these magnetic latitudes for a given geographic location are computed using a model of the geomagnetic field. In the present study, we use the thirteenth generation IGRF (International Geomagnetic Reference Field) for 1900 to 2025 (Alken et al. 2021) and the gufm1 model for before 1900 (Jackson, Jonkers & Walker 2000).

For auroral studies (e.g. Lockwood & Barnard 2015; Kataoka & Nakano 2021), dip geomagnetic latitudes have sometimes been used. These are given by a simple relation to the inclination of the field at Earth's surface (the angle of the field with respect to the vertical),  $I$

$$\Lambda_D = \tan^{-1} \left( \frac{\tan(I)}{2} \right) \quad (2)$$

This has often been used in historical studies of aurora (e.g. Lockwood & Barnard 2015), because of the ease of splining together values from models of the field used to compute the  $I$  values in different epochs. In addition, the differences between  $\Lambda_D$ , as defined by equation (2) and other magnetic latitude estimates stay relatively constant for a limited region of study. However, other studies have found that other geomagnetic latitudes better describe auroral morphology (e.g. Kataoka & Nakano 2021).

Magnetic Apex coordinates are calculated by tracing along magnetic field lines of the magnetic field model (in this case IGRF but splined to values from gufm1 for before 1900), from the point in question,  $P$ , to the highest point above the Earth (the apex) allowing for the deformation of the Earth's surface from a spherical form. The field line apex is at a geodetic height,  $h_a$  and the point in question is at a geodetic height  $h$ . The Modified Apex (MA) latitude,  $\Lambda_A$ , is defined relative to a constant reference height  $h_r$  by

$$\Lambda_A = \pm \cos^{-1} \left( \frac{R_E + h_r}{R_E + h_a} \right)^{1/2} \quad (3)$$

where  $R_E$  is the mean radius of the Earth. The sign is positive in the Northern magnetic hemisphere and negative for the Southern. The QD latitude is very similar to  $\Lambda_A$  but is defined relative to the geodetic height of the point  $P$ ,  $h_p$ .

$$\Lambda_M = \pm \cos^{-1} \left( \frac{R_E + h_p}{R_E + h_a} \right)^{1/2} \quad (4)$$

Hence, MA and QD latitudes are very similar; however, MA latitudes do not depend on the height of the point  $P$  (being referred to a constant altitude,  $h_r$ ). For  $h_r = h_p$  the two are the same but diverge if  $h_r > h_p$ . QD coordinates are useful for phenomena with a specific height profile because they allow for  $h_p$  and do not depend on a defined reference height. Reviews of MA and QD coordinates have been given by Richmond (1995) and Laundal & Richmond (2017).

Fig. 4 compares maps of dip  $\Lambda_D$  and QD  $\Lambda_M$  latitudes for an example year of 2015. It can be seen that the two are very similar at equatorial latitudes (values between  $-20^\circ$  and  $+20^\circ$ ) but the differences grow at higher latitudes. These differences are particularly severe in the Southern hemisphere, where the South Atlantic Anomaly (SAA) generates a large feature in  $\Lambda_D$  that is absent in  $\Lambda_M$ .

In this paper, we use QD latitudes  $\Lambda_M$  based on a join of magnetic field models IGRF and gufm1 in the following manner. We zero pad the IGRF spherical harmonic coefficients to match the maximum spherical harmonic degree (14) of gufm1, and then linearly taper the coefficients of gufm1 for 1890 to 1900 to those of IGRF at 1900 to prevent a step change in their values at the join. We then sample these combined model coefficients at the appropriate times to rebuild the cubic spline time basis of gufm1, ensuring that the linear

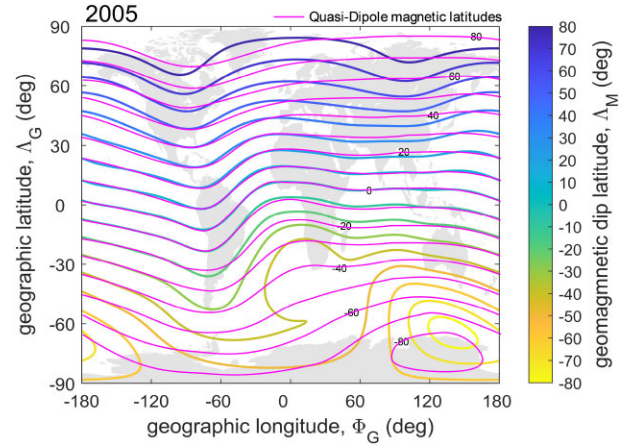


**Figure 4.** A comparison of dip geomagnetic latitudes  $\Lambda_D$  and QD geomagnetic latitudes  $\Lambda_M$  for an example year (2015). Contours,  $10^\circ$  apart, are shown of  $\Lambda_M$  (in mauve) and  $\Lambda_D$  (coloured according to the scale) on a Mercator map projection (as a function of geographic longitude  $\Phi_G$  and latitude  $\Lambda_G$ ).

time variation of IGRF is still retained after 1900. We compute  $\Lambda_M$  values using this field model with a modified version of the ‘Apexpy’ software (Emmert, Richmond & Drob 2010; van der Meeren et al. 2023).

That  $\Lambda_M$  orders particle precipitation more accurately than  $\Lambda_D$  is demonstrated by Fig. 5, which compares contours of  $\Lambda_M$  with energetic electron precipitation observed by the PROBA-V spacecraft at an altitude of 830 km. These electrons are in the energy range 0.5–0.6 MeV, which means they were trapped particles in the outer radiation belt and ring current that have been scattered into the loss cone. Parts A and B of Fig. 5 are global maps derived over periods of 28 d immediately before and after the St. Patrick’s Day storm presented in Figs 2 and 3. Antonova et al. (2018) argue that the auroral oval maps to the outer ring current and the outer part of the outer radiation belt, rather than the plasma sheet as often assumed. That is consistent with Fig. 5, in that 95.4 per cent of all the auroral observations used in this paper are between the two mauve lines shown. In addition, the black points show the locations of the auroral samples in the interval over which each precipitation map was compiled. Parts A and B are for, respectively, before and after the St Patrick’s Day storm and the increase in particle fluxes caused by the storm is apparent, as is the equatorward expansion of the aurora. Both parts show a major feature in the SAA, where particles precipitate because the loss cone width in pitch angle is increased by the low field strengths. These electrons are considerably more energetic (by a factor of order 50) than those that excite most auroras, which are typically in the 1 to 10 keV range. However, being so energetic means that their trajectories are close to field-aligned (field perpendicular convection during flight times is negligible) and we can see that at auroral latitudes they are well-ordered by the  $\Lambda_M$  contours. Studies using lower energy electrons show that these auroral bands of high-energy electrons coincide closely with the locations of auroral electron precipitation seen by the DMSP (Defense Meteorological Satellite Program) satellites at similar altitudes (Liu et al. 2024). These authors also identify the auroral oval over a 3 year interval using data on high-frequency magnetic fluctuations detected by AC Vector Magnetometer (ACMag) instrument on the Fengyun-3E satellite and show it to be in the same location as the energetic electron precipitation and auroral observations shown in Fig. 5.

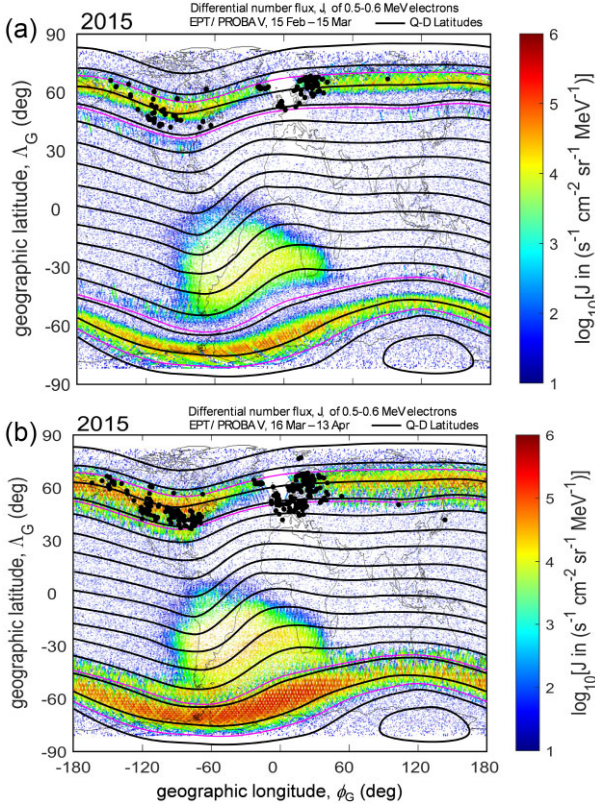


**Figure 5.** Ordering of particle precipitation by QD latitude,  $\Lambda_M$ . Contours of  $\Lambda_M$  for 2015 are shown in black as a function of geographic longitude  $\phi_G$  and latitude  $\Lambda_G$ . The coloured pixels give the differential number flux,  $J$ , of precipitating electrons in the energy range 0.5–0.6 MeV, as detected by the Energetic Particle Telescope on the PROBA-V satellite (Cyamukungu et al. 2014) over the intervals **A** 2015 February 15–March 15 and **B** March 16–April 13 (Pierrard & Lopez Rosson 2016), which are, respectively, before and after the ‘St Patrick’s Day’ geomagnetic storm. The mauve contours are the  $2\sigma$  points of the total distribution of  $\Lambda_M$  values of auroral observations derived from the catalogue of Northern-hemisphere observations for 1650–2024 used in this paper. The black dots are area-combined samples of auroral observations in the same interval as used to compile the map of electron precipitation.

The orange lines in Fig. 3 are contours of constant  $\Lambda_M$  and show that during the St. Patrick’s Day event, the aurora observed in the VIIRS DNB images are largely between  $\Lambda_M = 60^\circ$  and  $\Lambda_M = 70^\circ$ . This shows that  $\Lambda_M$  is effective in ordering the aurora, but we need to remember that the composite of images was taken over an extended interval of about 24 h at the peak of the storm. Hence, variations in the latitude of the aurora with time will appear as longitudinal variations in the image composite. Fig. 2B shows that the peak in mid-latitude  $aa_H$  index during the storm was at 18:00 UTC on 17 March 2015. Part C shows that the peak of the storm in the ring current (the minimum in the  $Dcx$  index) was later at 23 hrs UTC, as expected for the ring current growth time. The image in the composite shown in Fig. 3 recorded at 18:00 UT is that over mid-Siberia, in which aurora extends down to near  $\Lambda_M = 52^\circ$  in the image and mid-latitude aurora was recorded at this time at about  $3^\circ$  equatorward of this point at the ISTP SB RAS Geophysical Observatory (GPhO), slightly west of Irkutsk (Mikhalev 2019).

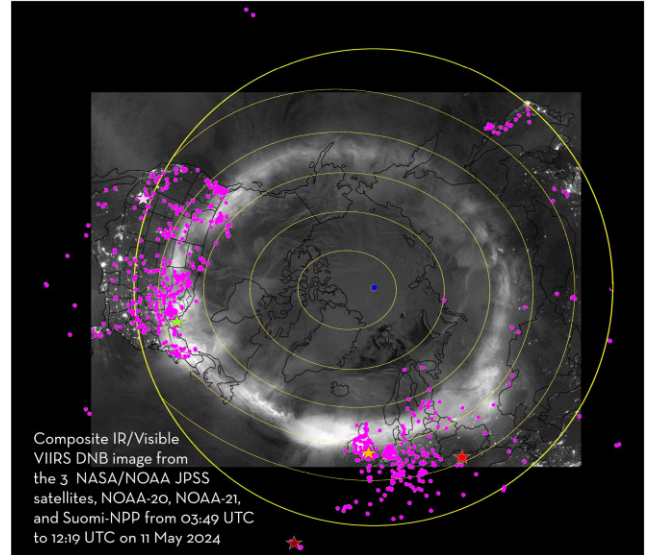


**Figure 6.** Area-combined auroral samples (mauve points) mapped onto a composite Near-IR/Visible DNB image for the Northern hemisphere auroral oval during the 2024 May 10–11 event. This composite is made from images from 3 satellites (unlike Fig. 3, which is made from just one): the NOAA/NASA JPSS satellites, NOAA-20, NOAA-21, and Suomi-NPP. The mauve dots are locations from which aurora was reported from the ground on 10 and 11 May 2024 and the orange contours are QD geomagnetic latitudes,  $\Lambda_M$ , of  $[40^\circ:10^\circ:80^\circ]$  for that date. The yellow circle is at geographic latitude  $\Lambda_G = 35^\circ$  and enables comparison with Fig. 3. The coloured stars are the locations from where the images shown in Fig. 7 were recorded. Image courtesy the VIIRS Imagery and Visualization Team, CIRA, Colorado State University, USA.

## 4 OBSERVATIONS

### 4.1 The major auroral event of 2024 May 10–11

Fig. 1 B shows a map of the locations of the 841 area-combined observation samples for the nights of 2024 March 10 and 11 (derived from 1611 reports). Like part A of the figure, the distribution shows a dearth of observations in Siberia. At all longitudes  $\phi_G$ , the range of geographic latitudes  $\Lambda_G$  is increased in Fig. 1 A by the secular changes in the geomagnetic field that alters the geomagnetic latitude at  $\Lambda_M$  at given geographic coordinates ( $\Lambda_G, \phi_G$ ) as well as by the greater range of geomagnetic activity levels. Nevertheless, an obvious feature is that middle and lower auroral latitudes seen in A are present in B but the higher latitude observations seen in A are missing in B. Specifically, in both panels there observations from the shores and islands of the Caribbean, USA, southern Canada, the UK, Central Europe, Southern Fennoscandia and Japan. However, observations from Alaska, northern Canada, Greenland, Iceland, Faroe Islands, and northern Fennoscandia that are present in part A are not seen in B.

Fig. 6 shows a composite of VIIRS DNB images during the 2024 May storm. Because this composite is taken from identical instruments on three satellites (compared to the one used to make Fig. 3) it was compiled over a shorter interval of 8.5 h and there is not a simple aliasing of temporal variations with longitude. The aurora is again well-ordered by  $\Lambda_M$  and sits between  $\Lambda_M = 50^\circ$  and  $60^\circ$ , which is consistently  $10^\circ$  equatorward of the aurora during the St. Patrick’s storm, as seen in the corresponding images. As for the St. Patrick’s Day storm, there are very few ground-based observation





**Figure 7.** Images from the night of 2024 May 10–11 from the locations marked by coloured stars in Fig. 6. **A** predominantly green aurora photographed from Barrie, Ontario, Canada (coordinates  $\Lambda_G = 44.38^\circ$  N,  $\phi_G = -79.7^\circ$  E – a QD magnetic latitude of  $\Lambda_M = 53.23^\circ$ ). Image credit: Will Dunn, copyright WD Photography. **B** green, blue and red aurora above Silbury Hill prehistoric mound, Wiltshire, England ( $\Lambda_G = 51.42^\circ$  N,  $\phi_G = -1.86^\circ$  E,  $\Lambda_M = 47.33^\circ$ ). Image credit: Nick Bull, copyright: Stonehenge Drones. **C** panoramic view of predominantly red aurora with a thin, low-altitude band of green, seen from Fundulea, Romania ( $\Lambda_G = 44.47^\circ$  N,  $\phi_G = 26.51^\circ$  E,  $\Lambda_M = 39.73^\circ$ ). Image credit: Maximilian Teodorescu, copyright Maximus Photography, Romania. **D** red and blue aurora mixture recorded in the Superstition Mountains, Arizona, USA ( $\Lambda_G = 33.48^\circ$  N,  $\phi_G = -111.46^\circ$  E,  $\Lambda_M = 40.47^\circ$ ). Image credit: Crystal Sibson copyright Crystal Sibson Photography. **E** red aurora seen at low elevations to the north from Breña Alta, looking over Santa Cruz de La Palma ( $\Lambda_G = 28.68^\circ$  N,  $\phi_G = -17.78^\circ$  E,  $\Lambda_M = 19.72^\circ$ ). Image credit and copyright: Giovanni Tessicini. All images reproduced with kind permission of the photographers.

locations (mauve dots) poleward of the main oval seen by VIIRS-DNB, some within that oval and many equatorward of it.

Fig. 7 shows five typical auroras seen on 2024 May 10 (when not an overhead coronal form). Their locations are marked by stars in Fig. 6, using the same identifying colours as in 7. Part **A** is an example of a full sky of green emission and is within the bright auroral band identified in the composite JPSS/VIIRS image. **B** is a clear example of the red emission from above the green. Between them there is blue visible, which is an emission from molecular nitrogen and may also be present at the same elevations as the red emission, giving a mauve tint to the red. This image was taken from the equatorward edge of the bright auroral band in the composite JPSS/VIIRS image. It is also taken very close to the geomagnetic latitude above which Grandin et al. (2024) found predominantly green and predominantly red were reported with roughly equal frequency, but below which predominantly red dominated the reports. At this point, we should note that colour is much more discernible in camera observations than by the unaided eye, and Hayakawa et al. (2025) note that this will have had an effect on the survey by Grandin et al. (2024). The

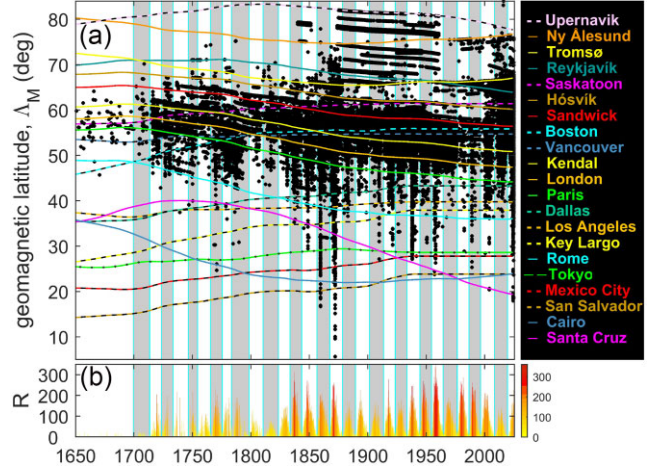


**Figure 8.** **A** A plot of the locations on a QD geomagnetic latitude ( $\Lambda_M$ ) of observer locations as a function of time for 194 201 independent area-combined samples from 219 244 observation records taken over the interval 1650 January–2024 July. The vertical cyan lines mark sunspot minima and grey and white shading denotes, respectively, even- and odd-numbered sunspot cycles. The various coloured lines give the variation of  $\Lambda_M$  with time for several selected sites (named on the right-hand side), computed from the spline of gufm1 and IGRF geomagnetic field models. **B** CR means of sunspot number,  $R$  shown in a bar-chart format where the histogram bars are coloured according to their height.

green just can be seen in **C** at the lowest altitudes but not in **D**, which are from very similar magnetic latitudes considerably below that of the bright auroral band in the composite JPSS/VIIRS image. Time-lapse movies and sequences of stills from these latitudes on this night show that this faint green lower edge to the red aurora forms and fades quite rapidly, and so this difference between these two images is more to do with temporal fluctuations than latitudinal structure. Lastly, **E** is from the Canary Islands and so is very close indeed to the lowest magnetic latitude observation on this day. If any green were present it was below the northern horizon and a red glow is seen to the north at low elevations. Part **E** and to a lesser extent **C** show a more monochromatic red than **D**, which shows a more mauve colour with larger associated emission of blue, which is particularly evident at the higher altitudes. However, in these cases one generally does not know the camera and image colour filters applied; hence such comparisons cannot be rigorous.

## 4.2 History of major auroral events

Fig. 8 shows the history of major events by plotting in Part **A** the geomagnetic latitude  $\Lambda_M$  of area-combined samples, as a function of date. The grey and white vertical bands mark even- and odd-numbered sunspot cycles, separated by vertical cyan lines at sunspot minima. The sunspot numbers are shown in Part **B**. Because of the secular change in the geomagnetic field, the  $\Lambda_M$  of specific sites have changed. These variations are plotted for a few selected sites to demonstrate the effects. Dashed lines are for sites in the USA/Canada/West-Greenland ‘American’ longitude sector, whereas solid lines are sites at longitudes further east in the ‘Eurasian’ sector. The sites in the American sector have generally migrated poleward in geomagnetic latitude, whereas those in the Eurasian sector have generally migrated equatorward. The example sites are named to the right of part **A**.



Note that there are some early and isolated reports of aurora at low latitudes that are not included in Fig. 8. These are often based on ambiguously worded texts and of uncertain provenance. To eliminate these, we do not include reports if there are no other reports on the same night at latitudes below the  $2\sigma$  point of the distribution of  $\Lambda_M$  values (discussed in Section 3.3). There are also some later low-latitude reports of ‘aurora’ in newspapers that are not included because they almost certainly originated from reports of disruption to telegraph systems. These are discussed in relation to the specific events studied in Section 4.4.

The 2024 May event is at the right-hand edge of the plot and the left-hand edge of the plot is during the Maunder minimum when observations were few and at higher  $\Lambda_M$  values. The Dalton minimum (c.1800–1825) has a clear signature with fewer auroral observations, especially at lower magnetic latitudes. Indeed, this solar minimum is so-named as it was first noted by John Dalton in his auroral observations (Silverman & Hayakawa 2021). The weaker secular solar minimum around 1900 is also accompanied by fewer observations at lower latitudes.

In addition to these minima, there is a general trend to lower latitudes as sunspot numbers increase through the period. However, it is hard to discriminate between the effects of solar variability and of the magnetic latitudes variations of locations with a population able and willing to record auroral observations. Eurasian observations are present throughout the interval, and European centres of population have migrated to lower geomagnetic latitudes: this is a big factor in the change seen in Fig. 8. Observers in the American sector have been moved in the opposite direction in magnetic latitude by the change in the geomagnetic field but there are big changes in the numbers and distribution of potential observers. The Mayflower arrived in America in 1620 and the first auroral observation in our data base is from 1715 in the New England area (Boston). Subsequently, that region moved to higher geomagnetic latitudes and the effect of that is clear in the data and the (magnetic) latitudinal width of the region of observations spread with increased population numbers (of individuals likely to record and aurora). That spread was largely to higher magnetic latitudes (i.e. up into Canada) and observations from the southern American states remained sporadic until about 1900 when the latitude spread suddenly increased to reach modern values, probably due to the establishment of the US national weather service in 1870 and the rapid growth of telegraph systems over the interval 1844–1900.

There are other changes to note. Observations in the American sector dropped dramatically after 1950 and only recovered with the growth of the internet, and the effect of that can be seen in Fig. 8. In this paper, we are concerned with extreme excursions of the aurora to low latitudes, and not the average location of aurora. Nevertheless, that we have observations from all longitudes is important because not all events are global in their greatest latitude extent. For example, the Carrington event aurora of 1859 was seen down to  $\Lambda_M$  of  $18.40^\circ$  in the American sector (the sightings listed in Table 2) but only  $23.75^\circ$  in the European sector (a sighting report from Senegal is often reported in newspapers but no details are given and so this is most likely a reference to a sighting from a ship off the Atlantic coast of West Africa at  $\Lambda_M = 24.14^\circ$  listed in the Kimball (1960) catalogue). What is interesting is that this event was recorded from almost all latitudes in both continents, even though routine observations were only made at a few geophysical observatories north of  $\Lambda_M$  of about  $60^\circ$  at that time.

Fig. 9 is the same as Fig. 8, but expanded to cover just the modern era (2013 January–2024 June). The intervals cover the peaks of cycles 24 and 25 and the minimum between them, as shown by the lower

panel, part B. Panel A reveals the annual variation in samples that we expect because of the effect of sunlight on the detectability of aurora. The solid vertical blue lines have been added to mark the summer solstice for these Northern-hemisphere data, and the vertical blue dashed lines mark the winter solstice. The expected annual variation is present, with a clear minimum in occurrence around the summer solstices, particularly at higher latitudes. There is also a clear semi-annual variation, with peak occurrence being at the equinoxes.

The semi-annual variations in geomagnetic activity are well understood in terms of the dipole tilt effect on solar-wind magnetosphere coupling, known as the Russell-McPherron effect (Russell & McPherron 1973; Cliver, Kamide & Ling 2002; O’Brien & McPherron 2002; Balan et al. 2017). A variety of tests have shown conclusively that this is the causal mechanism, one of the most compelling being that the favoured equinox depends on the polarity of the Y-component of the interplanetary magnetic field (IMF), which is a unique prediction of the Russell-McPherron theory (Zhao & Zong 2012; Lockwood et al. 2020a, b, c).

Fig. 10 shows the semi-annual variations in the number of samples at geomagnetic latitudes below 5 different thresholds for the whole data set (1650 January–2024 July). All show clear peaks around the March and September equinoxes. In all cases, the March equinox peak is slightly lower and broader than the September one. For the  $90^\circ$  threshold (all samples) there are fewer samples around the June solstice than the December solstice, as expected because of the reduced opportunity to observe aurorae caused by daylight. This difference decays with the latitude threshold and is negligible at  $50^\circ$  and lower. This behaviour can also be identified in the annual variations visible in Fig. 9. We conclude that the annual variation due to the axial tilt of the Earth effect on sunlight illumination has negligible influence on the auroral occurrence at magnetic latitudes below about  $50^\circ$ . Fig. 6 of Lockwood et al. (2020a) shows there is very little difference in the occurrence of large geomagnetic disturbances at the solstices, as is found here for auroral disturbances that reach to magnetic latitudes below  $50^\circ$ . More detailed comparison of the semi-annual variations in auroral and geomagnetic activity will be presented in a later paper.

#### 4.3 The distribution of geomagnetic latitudes of auroral events

Fig. 11 A is a histogram of the distribution of the geomagnetic QD latitudes of area-combined auroral samples,  $\Lambda_M$ , for the entire 374.5-yr period (1650 January–2024 July). The solid vertical mauve lines give the  $2\sigma$  points of the distribution (i.e. the 2.5 and 97.5 percentiles), which were plotted on the world maps in both hemispheres in Fig. 5.

It can be seen that, above the mode value in particular, the distribution is not smooth: this is expected because of the observations at the highest latitudes are from regions of very low population density and largely come from a few research stations. In addition, the intervals covered by these observations are short and data from summer months are almost entirely missing because of sunlight. The data that are available suggest the distribution is rather asymmetric, with the mode at a considerably lower value than the mean and the latitudinal width above the mode value being considerably greater than below the mode.

However, these problems are much reduced at lower latitudes because below the mode value the latitudinal distribution of potential observers is essentially continuous. Here the distribution is relatively smooth. Part B of Fig. 11 is a detail of the low-latitude tail of the distribution. The small number of the samples in this extreme tail of the distribution mean that the uneven geographic distribution of potential observers is having an effect. However, below a marked

**Table 2.** Great auroral events, ranked by the lowest QD geomagnetic latitude,  $\Lambda_M$ , from which aurora was observed. Columns from left to right give: 1. The rank. 2. Date. 3. The minimum  $\Lambda_M$  ( $[\Lambda_M]_{min}$ ) at which aurora was observed. 4. The number of area-combined samples  $N$  on that date with  $\Lambda_M < 31^\circ$ . 5. The separation in magnetic latitude of the lowest two  $\Lambda_M$  sample sites on that night  $\Delta\Lambda_M$ . 6. The site of the minimum  $[\Lambda_M]_{min}$  observation. 7. The minimum value of the  $Dcx$  index during the associated geomagnetic storm (values in square brackets are estimates of  $Dcx$  for events for which no  $Dcx$  value is available and 'n.a.' stands for 'none available' and means neither a  $Dcx$  value nor a  $Dcx$  index value during the event. 8. The peak  $aa_H$  index value during the event. 9. A note or name by which the event is often referred to. 10. Some example references to papers in the literature (of which there are often a great many others) that discuss the event in general. Note that the lowest-latitude observations on 2024 May 10/11, 2023 April 23, and 1950 August 19 (marked with an asterisk) were made using a camera: the implications of this for the May event are discussed in the text.

Rank	2 Date	3 Minimum $\Lambda_M$	4 $N$ $\Lambda_M < 31^\circ$	5 $\Delta\Lambda_M$ ( $^\circ$ )	6 Site of minimum $\Lambda_M$	7 Minimum $Dcx$ (nT)	8 Maximum $aa_H$ (nT)	9 Note	10 Refs.
1	1872-Feb-4	5.85	54	3.86	Khartoum, Sudan	[< -834]	626a		Berrilli & Giovannelli (2022), Silverman (2008)
2	1859-Aug-28	16.68	5	0.22	Panama	[< -484]	n.a.	Precursor to Carrington event	Hayakawa et al. (2023c), Hayakawa et al. (2018a)
3	2024-May-11	18.08	12	0.43	Ad-Dahiliyah, Oman*	-390	521	2024 May event, Day 2	Green & Boarden (2006), Hayakawa et al. (2022)
4	1859-Sept-2	18.40	24	0.20	La Unión & ships 'Sabine' & 'St Mary's'	[1000±150]	n.a.	Carrington event – Day 2	Hayakawa et al. (2025) Silverman (2006), Hayakawa et al. (2022) Green & Boarden (2006)
5	1859-Sept-1	18.60	14	5.14	ship 'St Mary's' (off El Salvador coast)	[-1000±150]	n.a.	Carrington event – Day 1	González-Esparza & Cuevas-Cardona (2018) Hayakawa et al. (2019a), Love et al. (2024) Silverman (2006), Hayakawa et al. (2018b) Green & Boarden (2006)
6	2024-May-10	19.12	16	0.58	Mogán, Gran Canaria*	-390 (0.0031 per cent)	521	2024 May event, Day 1	Hayakawa et al. (2019a), Love et al. (2024)
7	2003-Nov-20	20.41	4	0.22	Mount Teide, Tenerife	-418 (0.0021 per cent)	564	ICR after Halloween storms	Hayakawa et al. (2025)
8	1870-Oct-24	22.03	9	2.14	Giza, Cairo, Egypt	[n.a.]	368	we suggest <i>Donati event</i>	Vázquez & Vázquez (2010)
9	1957-Jan-21	23.73	2	0.68	Arrecife, Lanzarote	-255 (0.0641 per cent)	416	IGY January storm	Vázquez & Vázquez (2010), Hayakawa et al. (2023a)
10	1872-Feb-5	24.08	1	8.38	Shaoxing, Zhejiang, China	[n.a.]	626	Day after the 1872 February event	Hayakawa et al. (2018a)
11	1989-Mar-13	25.30	3	1.24	Dominica & Honduras	-564 (0 per cent)	722	Quebec power outage storm	Boteler (2019), Allen et al. (1989)
12	1958-Feb-11	26.28	8	0.93	Oguri, Japan	-421 (0.0017 per cent)	503	IGY storm	Hayakawa et al. (2023a)
13	1938-Jan-25	26.48	21	0.73	Tataouine, Tunisia	-336 (0.0090 per cent)	656	the Fátima Storm	Hayakawa et al. (2021)
14	1909-Sept-25	27.17	0	1.36	Matsuyama, Japan	[595]	576		Silverman (1995), Hayakawa et al. (2019b)
15	1941-Sept-18	27.75	1	5.44	Tunis, Tunisia	-404 (0.0026 per cent)	459	the 'geomagnetic blitz'	Love & Coisson (2016), McNish (1941)
16	2023-Apr-23	28.05	2	1.86	Hanle, Ladakh India*	-208 (0.0828 per cent)	205		Vichare et al. (2024)
17	2000-Jul-14	28.20	4	0.05	Mexico City	-295 (0.0197 per cent)	352	The Bastille storm	Kubota et al. (2017), Livesey (2000)
18	1982-Jul-13	28.84	2	0.01	Malta & Sardinia	-325 (0.0113 per cent)	447		Livesey (1984)
19	1848-Nov-17	29.53	3	2.53	St Croix	n.a.	n.a.	New York Railroad	Lang (1849), Valach et al. (2019)
20	1921-May-14	30.21	3	0.02	east and west tips of Jamaica	[-907±132]	831	Superstorm	Silverman & Cliver (2001), Carapiperis (1956)
21	1950-Aug-19	30.84	1	0.68	Spetses, Greece*	-260 (0.0373 per cent)	202	Photographic auroral report	Hapgood (2019), Love et al. (2019a) Abbott & Chapman (1959)

\*This peak  $aa_H$  value may be a slight underestimate because data from the Greenwich magnetometer are missing during this event.

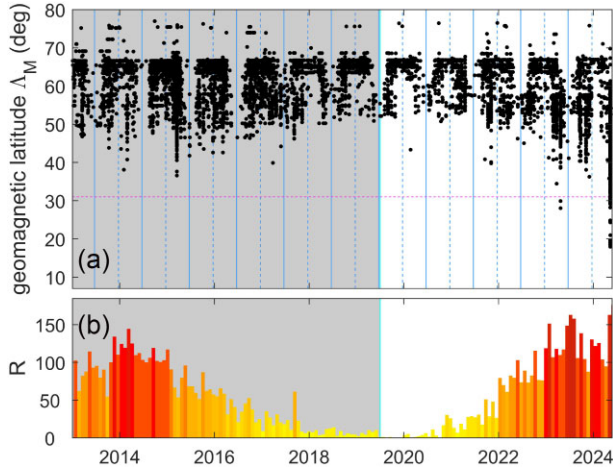


**Figure 9.** Same as Fig. 8 but for the interval 2013 January to 2024 July, covering approximately one solar cycle. In part **A** vertical solid and dashed blue lines have been added marking, respectively, the June and December solstices and a mauve horizontal dashed line marking the  $31^\circ$ -threshold for an extreme event that is adopted here.

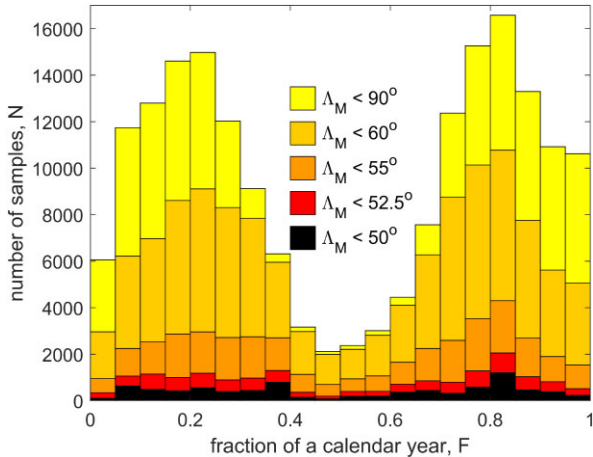


**Figure 10.** Annual variations seen in histograms of numbers of samples in bins of a fraction of a year  $F$  that are 0.05 wide. The shading from yellow to black is for samples with  $\Lambda_M < 90^\circ$  (i.e. all samples),  $\Lambda_M < 60^\circ$ ,  $\Lambda_M < 55^\circ$ ,  $\Lambda_M < 52.5^\circ$  and  $\Lambda_M < 50^\circ$ .

peak at  $\Lambda_M = 31^\circ$  the distribution is close to an exponential in form. This is demonstrated by the orange line in **B**, which is the best-fitting exponential to values at  $\Lambda_M < 45^\circ$ , given by  $ae^{(b\Lambda_M)}$  where  $a = 0.058$  and  $b = 0.216$ . Part **C** and **D** are the cumulative distribution functions (CDFs) for the same data as in **A** and **B**, respectively.

We are interested in this paper in excursions of aurora to low latitudes. The mode of the distribution in Fig. 11A is  $57^\circ$ , the median is  $57.73^\circ$  and the mean is  $59.86^\circ$ . The  $1\sigma$ ,  $2\sigma$ , and  $3\sigma$ , points of the distribution equatorward of the mean are at  $54.03^\circ$ ,  $47.63^\circ$ , and  $31.36^\circ$ , respectively. As the distribution of  $\Lambda_M$  values below  $31^\circ$  is close to an exponential in form, and so seemingly not greatly influenced by the geographic distribution of potential observers, we here define this geomagnetic latitude to be the low-latitude threshold to define an extreme event. This threshold is shown by the vertical dashed mauve lines in Fig. 11 and the area-combined samples at  $\Lambda_M$  below this threshold are just 0.126 per cent of the total data set. Note that our threshold is very slightly lower than the lower  $3\sigma$  point of the distribution. As discussed below, the pattern of population

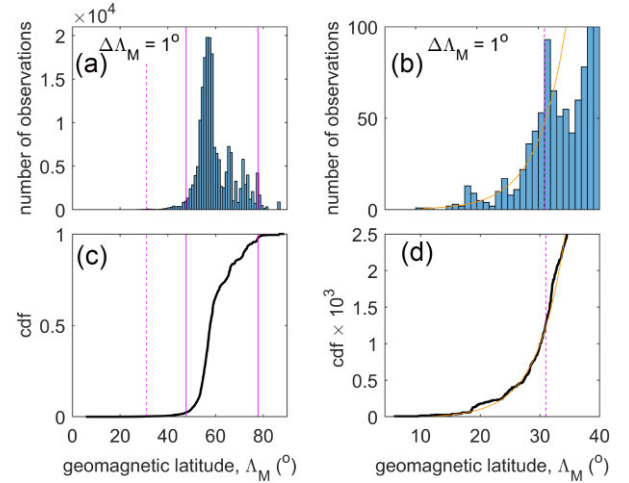


**Figure 11.** Distributions of the number of area-combined samples,  $N$  with QD geomagnetic latitude,  $\Lambda_M$ . **A** is a histogram of the full distribution in bins of  $\Lambda_M$  that are  $\Delta\Lambda_M = 1^\circ$  degree wide. **B** Detail of the low latitude tail of the distribution shown in **A** with the orange line being the best-fitting exponential rise of the distribution at  $\Lambda_M < 45^\circ$ , which is given by  $ae^{(b\Lambda_M)}$  where  $a = 0.058$  and  $b = 0.216$ . Part **C** is the CDF corresponding to **A**: the solid vertical mauve lines are the  $2\sigma$  points of the distribution. Part **D** is the CDF corresponding to **B** and the orange line again shows the best exponential fit. The vertical dashed line in all plots is at  $\Lambda_M = 31^\circ$  and marks the point where the distribution departs from the exponential. This is taken in this paper to be the threshold latitude for an extreme event. The CDF at this threshold shows that below this latitude are just 0.126 per cent of auroral sightings. The median auroral latitude is  $57.023^\circ$ , the  $1\sigma$  range is  $54.03$  to  $68.01^\circ$ , the  $2\sigma$  range is  $47.63$  to  $77.76^\circ$  and the  $3\sigma$  range is  $31.36$  to  $86.55^\circ$ .

density around the world minimizes the effects of variations in the geographic locations of the  $31^\circ$   $\Lambda_M$  contour, which is another reason why this value is chosen as the threshold that defines extreme events.

Fig. 12 plots as black dots on a Northern-hemisphere map where extremely low-latitude auroral sightings have been made since 1650. Part **A** shows all observation locations where  $\Lambda_M \leq 31^\circ$ . On the map are also plotted the  $\Lambda_M = 31^\circ$  contours for years 50 yr apart between 1650 and 2000. In Part **B** the observation locations just poleward of the  $\Lambda_M = 31^\circ$  contour are plotted on a map of the population density in the year 2022. This population map will obviously have changed considerably over the years, in particular with increasing numbers of individuals per unit area, but also with some spread in the locations where significant numbers of people live. However, a modern map is sufficient for our illustrative purposes. Both panels show that there is a clear correlation between where people live and where these extremely low-latitude aurora were observed. However, in Part **B** it can be seen that many of the observations just poleward of  $\Lambda_M = 31^\circ$  threshold are on the northern edge of a region of little-to-no population, in particular the Gobi Desert in China, the Sahara desert in Africa and the South Caribbean Sea between Cuba/Jamaica and the continent of South America.

Fig. 12 shows that large numbers of observations come from regions of high population, both below and just above the  $\Lambda_M = 31^\circ$  threshold; however, there is a complex interplay between the  $\Lambda_M = 31^\circ$  contour and some longitudinally extended boundaries of regions of high population density. Integrating the population along the contours of  $\Lambda_M$  just above  $31^\circ$  provides an explanation of the fluctuations in the numbers of auroral samples to the right of the vertical mauve dashed line in Fig. 11B. Comparing the two parts if Fig. 12 shows that observations that were made south of  $\Lambda_M = 31^\circ$ ,



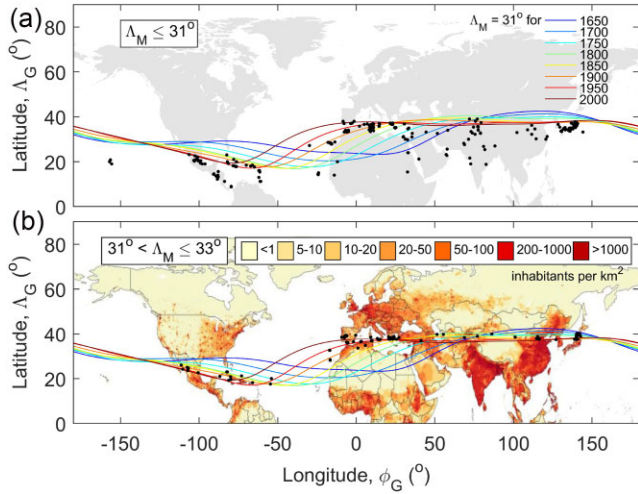


**Figure 12.** Maps of **A** locations of observations at geomagnetic QD latitudes below  $31^\circ$  (black points) and **B** of observations at low latitudes that do not quite meet the  $\Lambda_M \leq 31^\circ$  criterion, being at  $31^\circ < \Lambda_M \leq 33^\circ$ . The coloured contours on both panels are of  $\Lambda_M = 31^\circ$  for the years of [1650:50:2000]. The map in Panel **B** shows the global population density (in individuals per  $\text{km}^2$ ) in modern times (2022) (Mathieu & Rod s-Guirao 2022).

are nearly all where high population density extends south to lower latitudes. It can be seen that the extreme low-latitude observations with  $\Lambda_M \leq 31^\circ$  were seen in high population areas such as (from east to west) as Japan; eastern China; two small sub-Himalayan regions near  $77^\circ\text{E}$  that include Xinjiang province in western China, Ladakh and Kashmir in India and northern Pakistan; the Middle East; the north-west coast of Africa and the Canary Islands; and Mexico and Central America.

The evolution of the  $\Lambda_M = 31^\circ$  contour over time is interesting because the biggest changes are over the Sahara and the middle Atlantic Ocean, where population numbers are small or zero. Even the smaller changes are mainly over the Gobi Desert or the Pacific Ocean. Hence, by chance, there is very little change in the  $\Lambda_M = 31^\circ$  contour location in the places where population density is high and so these the changes in magnetic latitude will have had a very limited effect on the probability of observing aurora. The main place where the secular change in the geomagnetic field may have altered the relationship of our threshold contour with population density is the Middle East and Arabia, where both population numbers and auroral observations are both quite low and spread thinly.

In Section 4.6 we reduce the interval of interest to 1790–2024.5 (i.e. from just before the Dalton minimum to 2024 June) for which only the yellow, orange and red contours of  $\Lambda_M = 31^\circ$  shown in Fig. 12 apply. It can be seen that this removes the Middle-East/Arabia area as one where the threshold contour has moved, which further reduces the effects of the changes in the location of the  $\Lambda_M = 31^\circ$  contour. Hence, our choice of  $\Lambda_M$  threshold also means that the secular change in the magnetic field has had only minimal effect on the general probability of observation of very low-latitude aurora, especially after 1790.

The date 1790 is useful because auroral reporting had reached modern levels by this date, with 1.48 records per night and reports on 38.64 per cent of nights. These numbers are close to those for modern data: for example, they are 1.65 and 38.73 per cent for 2000–2024.5. For the interval 1790–2024.5 the average number of reports per night is 2.32 and aurora is reported on 48.23 per cent of

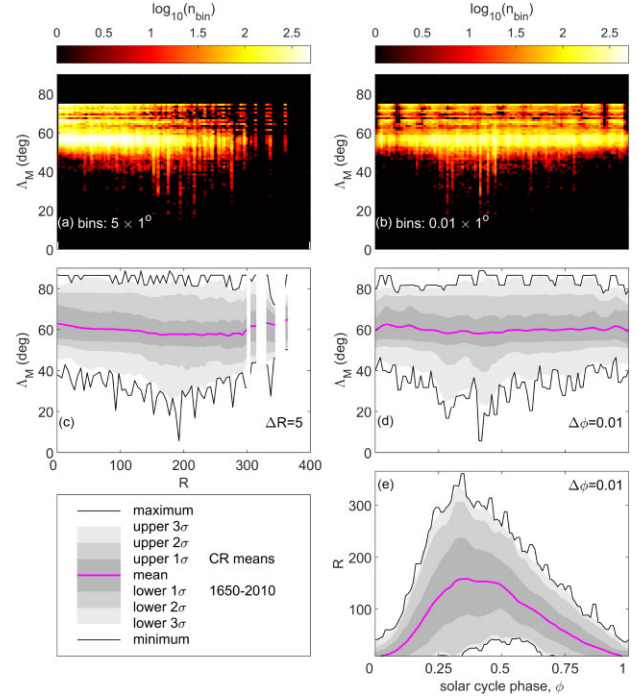


**Figure 13.** The variations of QD latitudes of the area-combined auroral samples,  $\Lambda_M$ , with sunspot number  $R$  and solar cycle phase  $\phi$  (where  $\phi = 0$  at the minimum in monthly  $R$  that marks the start of a cycle and  $\phi = 1$  at the sunspot minimum that marks its end). This plot is based on the full data set (1650–2024.5). Parts **A** and **B** are ‘data density plots’ (two-dimensional histograms). Part **A** shows the numbers of area-combined samples in bins that are  $1^\circ$  wide in  $\Lambda_M$  and 5 wide in  $R$ . **B** shows the numbers in bins that are again  $1^\circ$  wide in  $\Lambda_M$  and 0.01 wide in  $\phi$ . Parts **C** and **D** show the same data as **A** and **B** in a different format: **C** corresponds to **A** and shows the variation of the  $\Lambda_M$  distribution with  $R$  and part **D** corresponds to **B** and shows the variation of the  $\Lambda_M$  distribution with  $\phi$ . Part **E** shows the variation of the distribution of  $R$  as a function of  $\phi$ . In parts **C**, **D**, and **E**, the maximum and minimum of the  $\Lambda_M$  distribution are shown by black lines and the light grey, mid-grey and darker grey delineate values that are within, respectively, the  $\pm 3\sigma$ ,  $\pm 2\sigma$ , and  $\pm 1\sigma$  points of the distribution, the mean of which is shown by the mauve line.

nights. The first event after 1790 that meets our  $\Lambda_M < 31^\circ$  criterion is in 1848.

We have studied how the distribution of area-combined observations has varied with sunspot number and the phase of the solar cycle,  $\phi$ . We define  $\phi$  to be zero at each sunspot minimum and to be unity at the subsequent minimum, and to vary linearly with time over the cycle in-between. The results are shown in Fig. 13 for the full data set (1650–2024.5).

Panel **A** of Fig. 13 shows a ‘data density plot’ (a two-dimensional histogram) where the number of area-combined observations samples,  $n_{bin}$  is colour-coded for bins that are  $1^\circ$  wide in  $\Lambda_M$  and 5 wide in sunspot number  $R$ ; the colour coding being according to the scale given at the top. Panel **B** is the same for bins that are  $1^\circ$  wide in  $\Lambda_M$  and 0.01 wide in the solar cycle phase,  $\phi$ . Panels **C** and **D** show the same data in a different format. The mauve lines are the mean values of  $\Lambda_M$  as a function of  $R$  and  $\phi$ , respectively (in bins of width  $\Delta R = 1$  and  $\Delta \phi = 0.01$ ) and the light grey, mid-grey, and darker grey bands delineate  $\Lambda_M$  values that are within, respectively,  $\pm 3\sigma$ ,  $\pm 2\sigma$ , and  $\pm 1\sigma$  points of the distribution. The black lines are the maximum and minimum values of  $\Lambda_M$  in each bin.

Part **E** is in the same format as **C** and **D** but shows the variation of the distribution in  $R$  with  $\phi$ , using bins of  $\phi$  that are 0.01 wide. This plot shows the well-known behaviour that, on average, the solar cycle peaks at  $\phi = 0.33$  but it peaks earlier if the sunspot number is higher than average, and later than this if  $R$  is lower than average.

Parts **A** and **C** of Fig. 13 show that the aurora do shift to lower latitudes as  $R$  increases. At the highest latitudes the events become increasingly less frequent and are seen with only low frequency the largest  $R$ . Note, however, they are still seen. The mean of the distribution, and the lower  $3\sigma$ ,  $2\sigma$ , and  $1\sigma$ , points, all decrease with increasing  $R$ , up to about 250 where, rather surprisingly, they start to increase again. The lowest latitude reached is highly variable, reflecting the occurrence of a few extreme events. These events are most frequent and to lower latitudes at  $200 < R < 250$  but they are less common and do not reach as low latitudes if  $R$  is larger than this range. This behaviour is in good agreement with the occurrence of extreme events of geomagnetic activity, as reported by Owens et al. (2021).

Parts **B** and **D** of Fig. 13 show that all values, including the minima, are lower at sunspot maximum and that the largest excursions south almost always occur in the years around sunspot maximum. Again, this agrees with the occurrence of extreme events of geomagnetic activity reported by Owens et al. (2021).

#### 4.4 The greatest auroral events, in terms of the lowest geomagnetic latitudes reached

Between the Maunder and the Dalton minima, there are some scattered observations of aurora at latitudes below our threshold latitude of  $31^\circ$ . However, they are rare and isolated. For some of these nights the observation is the only one that was recorded, for others there are some others but these were all many degrees in magnetic latitude ( $\Delta\Lambda_M > 10^\circ$ ) poleward of the recorded low-latitude observation.

The first date for which we have records of auroral sightings from a large range of latitudes is 1848 November 17. For this date, our data base contains a total of 114 area-combined samples (at  $\Lambda_M$  between  $29.53^\circ$  and  $72.7^\circ$ ), with aurora seen throughout Europe and the United States. The lowest magnetic latitude observation was from the tiny island of St Croix of the British Virgin Islands in the southern Caribbean Sea ( $\Lambda_G = 17.72^\circ$  N,  $\phi_G = -64.84^\circ$  E, at that date  $\Lambda_M = 29.53^\circ$ ), reported by Sir Andrew Lang, the governor of the island, who provided a highly plausible description of a low-latitude red aurora in Monthly Notices (Lang 1849). This was the only observations on that date that meet the  $\Lambda_M \leq 31^\circ$  criterion ( $N = 1$ ). The nearest observation offers some confirmation and was from Havana in Cuba ( $\Lambda_G = 23.13^\circ$  N,  $\phi_G = -82.38^\circ$  E, at that date  $\Lambda_M = 32.06^\circ$ ) and so was just  $2.53^\circ$  poleward of the St Croix observation. The Havana observation was reported at the time in newspapers around the world, including the local ones in Cuba, and is listed in the catalogue of Fritz (1873). A range of latitudes reaching continuously down to the lowest point of observation is taken to show that St Croix, in this case, was not under a small isolated patch of mid-latitude aurora, which can occur – for example in localized SAR arcs. To limit this possibility, and also to help expunge faked reports and misreported reports, we here require that to be considered valid, the lowest latitude recorded cannot be more than ten degrees equatorward in magnetic latitude ( $\Delta\Lambda_M < 10^\circ$ ) than any other record on the same night. This may well remove some genuine low-latitude auroral results from the early years, but such isolated reports cannot be relied upon.

Because there are no events that meet this criterion before the Dalton minimum and because of the large change in  $\Lambda_M$  contour

location in the Middle-East and Arabia discussed in the last section, we restrict the detailed study of events to after 1790. Events that reached down to, or below, this magnetic latitude in this interval are listed in Table 2, in which they are ordered by the lowest  $\Lambda_M$  reached. To gain to an event classification, we require at least one other area-combined sample be within  $10^\circ$  in  $\Lambda_M$  of the sample at  $\Lambda_M \leq 31^\circ$ . The 1848 November 17 event that reached down to St Croix is event number 18 in the list of 21 events.

Note also that we use the quoted date for an event and consider the second (astronomical) night of a long-lived storm as a separate event. This applies to the Carrington event and to the 2024 May 10–11 event, both of which lasted for 2 d. For many observations, we know this is valid because the same observer records the observations on both days and/or gives the universal or local time of the observations. However, we need to recognize that some cases may be because the observer has moved the date forward by a day if the observation is made after local mid-night; in which case the Day 2 observation is misplaced and should be in the Day 1 data set. In both the 2024 May event and the Carrington event, the Day 2 aurora reaches slightly lower latitudes than that reached on Day 1.

Column 7 of Table 2 gives the minimum value of the geomagnetic  $D_{cx}$  index during the associated geomagnetic storm. For some events before 1932, we have estimates of the  $D_{st}$  index made by a variety of methods. One method employs the minimum geomagnetic latitude of the aurora (Yokoyama, Kamide & Miyaoka 1998), which is not the same thing as the minimum geomagnetic latitude of the observers. Although there is undoubtedly constraining information to be had from the equatorward auroral boundary (Blake et al. 2021), Hayakawa et al. (2023c) note that the method almost certainly gives  $D_{st}$  values that are unrealistically too large when extrapolation is extended to the very largest of auroral events. These  $D_{st}$  estimates are not appropriate for Table 2 because the reason for including minimum  $D_{cx}$  values and  $D_{st}$  estimates in the table is to compare with the minimum  $\Lambda_M$  values, and the two are not independent if the latter has been used to estimate the former. The values in square brackets are estimates of the storm's minimum  $D_{st}$  value: the letters 'n.a.' in square brackets are used if no such estimate is available. There have been a number of estimates of the minimum  $D_{st}$  value during the storm associated with the extreme auroral events of August/September 1859 and these vary between  $-800$  nT and about  $-1760$  nT. It is important to estimate hourly values (Siscoe, Crooker & Clauer 2006) to compare with  $D_{cx}$  values. The value quoted for these events in Table 2 ( $1000 \pm 150$ ) is derived from Love et al. (2024) and Cliver & Dietrich (2013): all estimates for this event come from the Colaba magnetogram and differ in the complexity of analysis applied to retrieve the information. The value for the 1921 May 14 event is given by Love et al. (2019b) and for the 1909 September 25 event (that does not quite meet our  $\Lambda_M \leq 31^\circ$  criterion) is from Hayakawa et al. (2019b). For the 1872 February 4 event, the value given is a  $D_{st}$  estimate by Hayakawa et al. (2023a) using data from one magnetometer station.

For many events, for example, that of 1921 May 14 (19 in the ranked order) the lowest latitude observation of aurora was made by known individuals and is well corroborated. In this case it was made by the staff of the Morant Point Lighthouse at the east tip of the island of Jamaica ( $\Lambda_G = 17.92^\circ$  N,  $\phi_G = -76.18^\circ$  E, at that date  $\Lambda_M = 30.36^\circ$ ) and recorded by the lighthouse superintendent, Mr C. Durrant. It was also seen by the staff of the Negril Point lighthouse at the west end of the island, which is at a magnetic latitude that is only marginally greater ( $\Lambda_G = 18.25^\circ$  N,  $\phi_G = -78.36^\circ$  E, at that date  $\Lambda_M = 30.27^\circ$ ). It was also recorded by the superintendent there, a Mr J.S. Brownhill. The aurora was also seen in Graham Town just

north-east of Kingston and mid-way between the two lighthouses and recorded in considerable detail by Lieutenant A.W. Tucker, who describes what we now recognize to be a diffuse red glow mixed with some rays of a green-line arc. In all three cases, the aurora was reported as being to the north. This was all recorded by Herbert Lyman in his survey of the event, published two months after the event in *Monthly Weather Review* (Lyman 1921). As well as there being three corroborating observations, there is an almost continuous distribution of sightings at greater  $\Lambda_M$  from observers on a trading ship south of Cuba, in Mexico, all throughout the USA, and in Southern Canada, France, England, Scotland, and Scandinavia. Hence, the auroral expansion down to the minimum latitude is very well defined in this case. However, we note there is an isolated report closer to the equator, from Apia in Samoa in the Southern hemisphere. However, this observation was in daylight and studying the newspapers from Honolulu reveals no mention of aurora, which would be expected as it is as a similar  $\Lambda_M$  (but in the northern rather than the southern magnetic hemisphere). Hence, in this case the minimum  $\Lambda_M$ , in the Northern hemisphere at least, is very well defined.

The event on July 2000 July 14, referred to as ‘Bastille Day’ storm, demonstrates a cautionary point about our survey. At the peak of that storm, an image taken by the Polar spacecraft UV imager showed aurora between magnetic latitudes of 26.24° N and 67.32° N over eastern America and the Caribbean. However, cloud cover was remarkably omnipresent in this area during the event and ground-based reports of observations are rare: our data set contains just 19 area-combined samples on this day. This was also at the time that newspaper reporting of aurora was in decline and social media reporting was in its infancy. Nevertheless, the ground-based observations do (just) meet our criteria. The lowest latitude observation was from Mexico City; however, this is only known because newspapers carried the story of people collecting in Chapultepec Park in the city ( $\Lambda_G = 19.42^\circ$  N,  $\phi_G = -99.19^\circ$  E, at that date  $\Lambda_M = 28.43^\circ$ ) to view what they thought was an alien invasion! This was later confirmed to be aurora by a nearby astronomical observatory. The next lowest magnetic latitude auroral report on that night was from Split, Croatia ( $\Lambda_G = 43.52^\circ$  N,  $\phi_G = 16.5^\circ$  E, at that date  $\Lambda_M = 37.94^\circ$ ), communicated to the British Astronomical Association by British tourists in the region (Livesey 2000). Hence, this event has a  $\Delta\Lambda_M$  value of 9.51° and is just under our threshold criterion. The point is that, despite the potential for observations over much of the Northern hemisphere, it is possible that our survey has missed an event at a time when reporting was low, and/or cloud cover was extensive at the longitude of mid-night MLT at the time of peak disturbance.

The 1909 September 25 event raises another important point about our survey. Silverman (1995) discounts a reported sighting on this night from Singapore ( $\Lambda_G 1.34^\circ$  N,  $\phi_G 103.83^\circ$  E). If valid, this report would give  $\Lambda_M$  of  $-7.69^\circ$ . However, this does not meet our  $|\delta\Lambda_M| < 10^\circ$  criterion, being more than 21° closer to the magnetic equator than the Matsuyama sighting. Silverman (1995) notes that this report originates only from a newspaper article and likely refers to a disruption of cable transmissions. Likewise, Silverman discounts a newspaper report from Shimla (formerly Simla), India on this day ( $\Lambda_G = 31.15^\circ$  N,  $\phi_G = 77.25^\circ$  E,  $\Lambda_M = 24.12^\circ$ ). This is because George C. Simpson (later Sir George and President of the Royal Meteorological Society) was working at the Indian Meteorological Service headquarters in Shimla at the time. He had a particular interest in geomagnetic and auroral events and always included them in national Meteorological reports. However, on this date he mentions no aurora, not only in Shimla but anywhere in India or Central Asia in general. In a letter to *Nature*, however, he does mention a

geomagnetic disturbance at Shimla during this night and it is likely that this too, at some stage, was wrongly interpreted as also revealing aurora. This report would otherwise be allowed by our criteria, but because Silverman questions it, we apply the precautionary approach and omit it. In the Southern hemisphere, the 1909 September event was seen widely in Australia but not in Indonesia, which you would expect were Singapore or Shimla really correct. That leaves the lowest confirmed geomagnetic latitude on this night as Niigata in Japan ( $\Lambda_G = 37.9^\circ$  N,  $\phi_G = 139.1^\circ$  E, at that date  $\Lambda_M = 31.12^\circ$ ). If the Shimla report were valid (and not another report of cable disruption, which is the most likely explanation) this would raise event 21 to 11 in the ranked order. This change is not important in itself but does remind us that single reports can alter the ranking order considerably.

We note that the event ranked #8 in the list, on 1870 October 24, has not been given a name. This event was reviewed by Vaquero et al. (2008) and a notable feature was that green auroral emission was seen at unusually low latitudes. Karl Friedrich Zöllner made spectroscopic observations of this event from Leipzig, Germany ( $\Lambda_M = 48.18^\circ$ ) that confirm considerable green emission there (Zöllner 1870). Although not the first such spectroscopic observation of aurora, Zöllner was a pioneer of astronomical photometry (Sterken & Staubermann 2000) and it would be appropriate to name the event after him. It might also be appropriate to name it after Giovanni Battista Donati, who observed the event and geomagnetic disturbance from Florence, Italy ( $\Lambda_M = 40.31^\circ$ ) and noted that the colour evolved from crimson to white (a common response of the human eye) and then to green. After observing this event and the 1872 February event, Donati suggested the term ‘cosmical meteorology’, which, in the modern form of ‘space weather’, is now a full and active discipline of science (Lockwood & Owens 2021). Sadly, Donati himself never got the chance to pursue the concept further as he contracted cholera while attending a conference in Vienna in August 1873 and died a month later, at age 46 (Clerke 1911). However, consistent with the discussion about the naming of storms below in relation to the storm of 1872 February 4, we here refer to this event as the ‘October 1870’ event.

Lastly on Table 2, we note that the lowest-latitude observations on 2024 May 10 and 11 (marked with an asterisk) were made using modern digital cameras. Later in this paper, Table 4 will classify how the low-latitude observations in the 2024 May events were made. Here we note that for these lowest latitude aurora, the observers did not state that they saw the aurora by naked eye, nor did they state that they did not. Hence, the visibility to the naked eye is not actually known in these cases. We also note that visibility to the naked eye covers a very wide range of luminance levels, as discussed in Section 2. On May 10 the lowest Q-D latitude in our data base where an observer reports seeing the aurora with the unaided eye is  $\Lambda_M = 19.70^\circ$  (at Santa Cruz de la Palma) and on May 11 it is  $\Lambda_M = 19.49^\circ$  (at Naalehu, Hawaii). This means that if aurora was genuinely unobservable with fully dark-attuned human eyes equatorward of these locations (which is not certain), 11 May would fall from 3<sup>rd</sup> to 5<sup>th</sup> in the ranking, whereas May 10 would remain at 6<sup>th</sup>. The effects of modern technology on the 2024 May event, including cameras, will be discussed in Section 4.7.

#### 4.5 The lowest magnetic latitude of auroral observations

The question of the lowest geomagnetic latitude from which aurora can be seen needs to be addressed. Fig. 4 shows that the QD and dip equators are almost identical, so the magnetic field is horizontal at the geomagnetic equator. For the field line to reach up into the magnetosphere, we have to move to non-zero  $|\Lambda_M|$ . We can get an estimate of how far we need to be from the magnetic equator



using invariant magnetic latitude,  $\Lambda_I$ , which is defined from  $L = 1/(\cos(\Lambda_I))^2$ , where for a dipole field,  $L$  is the geocentric height of the equatorial apex of the field line in units of Earth radii ( $R_E = 6370\text{km}$ ). For  $\Lambda_I = 10^\circ$ , this gives a maximum (apex) field line altitude  $h$  of just 198 km, which is below the ionosphere and can be discounted:  $\Lambda_I = 20^\circ$  gives  $h = 834\text{ km}$  ( $0.13R_E$ ) in the topside ionosphere,  $\Lambda_I = 30^\circ$  gives  $h = 2123\text{ km}$  ( $0.33R_E$ ),  $\Lambda_I = 40^\circ$  gives  $h = 4485\text{ km}$  ( $0.70R_E$ ) and  $\Lambda_I = 50^\circ$  gives  $h = 9047\text{ km}$  ( $1.42R_E$ ). Shiokawa et al. (2013) used ground-based and satellite observations to estimate that mid-latitude, storm-time, red aurora originated from magnetospheric populations of at  $L$  of about 2, which corresponds to  $\Lambda_I \approx 45^\circ$ . Hence, it is hard to conceive auroral precipitation at  $\Lambda_I$  below about  $30^\circ$ , although not impossible (Silverman & Cliver 2001).

However, these considerations relate to the magnetic latitude of coronal auroral forms, where the observer is close to being on the field line down which the causal particles precipitate. The lowest-latitude auroras in our data set are not coronal forms, they are viewed at low elevation angles ( $\beta$ ) from locations equatorward of the field lines on which the precipitation is occurring. To investigate how far equatorward of the low-latitude precipitation edge is possible (i.e. how large the offset in geomagnetic latitude between the observer and the field line of the precipitation can be), we use the dipole field geometry shown in fig. 9 of Hayakawa et al. (2023c). The altitude of the emission,  $h$  influences this calculation because higher altitude aurora can be seen from further away.

Megan Gillies et al. (2017) show that, in the auroral oval, the peak emission altitude for 630 nm red-line emission of atomic oxygen is near 220km; however, for mid-latitudes 630nm emission is expected from greater altitudes because of the lower energy part of the spectrum of causal broad-band electrons (BBE). Theoretical profiles given by Nagy, Roble & Hays (1970) (from the PhD thesis of Ray Roble) and Kataoka et al. (2024a) show peak emission is around 450-500km and that at altitudes of 600km and 1000km the intensity is, respectively, 1 and 2 orders of magnitude lower than at the peak. The emission altitude of mid-latitude storm-time red aurora has been studied by Kataoka et al. (2024b) using triangulation from different observation sites and they found it was detectable up to  $h$  of about 600 km. However, for the 2024 May event, Kataoka et al. (2024a) used images from citizen scientists and find emission from altitudes of  $1100 \pm 200\text{km}$  for an extended interval. However, we need to bear in mind that these authors use digital images and the maximum altitude could be lower for naked-eye observations. If we take the images to be made with ISO 3000 cameras, the theoretical profiles indicate this would lower the top emission altitude detectable by about 200–300 km. Hence, it may be possible to detect emission from up to 800 km by naked eye. Zero elevation would not be detectable and it is reasonable to assume that an elevation,  $\beta$  of at least  $5^\circ$  over the horizon, is needed to detect auroral luminosity.

We here use  $h = 800\text{ km}$  as a maximum altitude from which a human observer, under the most favourable conditions, could detect such an aurora. The formula needed to compute the latitude of observation  $\lambda_M$  for an observing elevation angle  $\beta$  and emission at an altitude  $h$  on a field line that reaches Earth's surface at QD latitude of  $\lambda_F$  is

$$\lambda_M = \left\{ \cos^{-1} \left( \frac{\cos \lambda_F}{a^{1/2}} \right) \right\} - \left\{ \frac{\pi}{2} - \beta - \sin^{-1} \left( \frac{\cos \beta}{a} \right) \right\} \quad (5)$$

where  $a = (R_E + h)/R_E$  and  $R_E$  is the radius of Earth's surface. The first term in 5 accounts for the difference in latitude between the point of emission and the latitude where the field line reaches the ground ( $\lambda_F$ ) and the second term accounts for the difference in latitude between the point of emission and the observer at  $\lambda_M$ .

**Table 3.** Values of QD latitude  $\Lambda_M$  from which an aurora could be observed at elevation  $\beta$  for emission along an auroral field line of QD latitude  $\Lambda_F$  at an altitude  $h$ .

$\Lambda_F(^{\circ})$	20	20	20	30	30	30	40	40	40
$h\text{ (km)}$	150	450	800	150	450	600	150	450	800
$\beta$									
$0^\circ$	9.4	3.8	0.3	18.8	12.2	8.0	28.4	21.3	16.5
$5^\circ$	13.5	8.2	4.9	22.9	16.7	12.5	32.5	25.7	21.0
$10^\circ$	15.9	11.6	8.7	25.3	20.1	16.3	35.0	29.1	24.8
$15^\circ$	17.4	14.2	11.8	26.8	22.6	19.4	35.5	31.7	27.9
$20^\circ$	18.4	16.1	14.3	27.8	25.5	21.9	37.5	33.6	30.4

Table 3 gives values of the QD latitude of a ground-based observer  $\lambda_M$  who is able to see aurora at an elevation  $\beta$  above the horizon for auroral precipitation down field lines of QD latitudes  $\Lambda_F$  of  $20^\circ$ ,  $30^\circ$ , and  $40^\circ$  and emission altitudes of  $h$  of 150, 450, and 800 km. These values are all approximate as they assume a dipole field model. The top row is the limit (zero elevation) but aurora would not be detectable and a higher  $\beta$  is required. The table shows that  $\Lambda_M$  is only below  $10^\circ$  for exceptionally high  $h$  and exceptionally low  $\Lambda_F$ . From observations Vichare et al. (2024) report an example of aurora detected at Hanle, India where  $(\Lambda_F - \Lambda_M) = 17^\circ$ , which is the largest confirmed value that we know of. We conclude that observations from  $\lambda_M$  below  $10^\circ$  will be very rare indeed and need careful checking.

The event of 1872 February 4 is generally agreed to be the most extensive auroral event known. This event was observed and recorded in some detail by many observers, including Father Angelo Secchi in Rome (Berrilli & Giovannelli 2022). Notably, Secchi used simultaneous observations by a wide variety of different instruments – he even noted some effects on global technological systems, in particular telegraph networks. This event has been termed the ‘Chapman-Silverman event’ after two of the scientists who later studied it in greater detail (e.g. Hayakawa et al. 2023a): we note the ‘Carrington event’ of 1859 is named after the scientist who observed it at the time rather than those who studied it later and hence prefer the term ‘1872 February event’. On the subject of naming storms, we note that the event of 10/11 2024 May has already been variously termed the ‘Mother’s Day storm’, the ‘Gannon storm’, the ‘Han Anniversary Storm’ and the ‘May-hem’ storm. As one has to remember the date that goes with each such name, this practice of naming storms has become unhelpful and confusing – the name ‘2024 May storm’ is unambiguous and informative.

The lowest magnetic latitude of a sighting in the 1872 February event is a matter of some debate. In our data base there are nine independent and credible reports of aurora on 1872 February 4 from Mumbai (Bombay) in India ( $\Lambda_G = 19.12^\circ\text{ N}$ ,  $\phi = 72.87^\circ\text{ E}$ , on that date  $\Lambda_M = 9.71^\circ$ ) and several reports from elsewhere in India and Pakistan. However, the lowest latitude report was conveyed to Pictet (1872) from Khartoum ( $\Lambda_G = 15.580^\circ\text{ N}$ ,  $\phi_G = 32.54^\circ\text{ E}$ , on that date  $\Lambda_M = 5.85^\circ$ ). This is a second-hand report but does appear credible; however it does imply very low elevation angle  $\beta$ , exceptionally low  $\Lambda_F$ , and a high emission altitude  $h$ . If we use  $h = 800\text{km}$ ,  $\beta = 5^\circ$ , and the Q-D latitude of Khartoum at the time of the 1872 February event ( $\Lambda_M = 5.85^\circ$ ), equation (5) gives that the precipitation on the equatorward edge of the aurora was at Q-D latitude of  $\Lambda_F = 21.3^\circ$ , which is a field line that reaches a maximum altitude of just 971 km at the magnetic equator, in other words the magnetospheric disturbance driving the precipitation must reach down to the topside ionosphere. Applying the same criteria to

the 2024 May event, the observations from Oman at  $\Lambda_M = 18.08^\circ$  give  $\Lambda_F = 36.6^\circ$ , which is a field line that reaches a maximum altitude of 3513 km at the magnetic equator. However, the Oman observations are of green line emission, which suggest a maximum altitude of only about  $h = 150$  km (Lee et al. 2017), which gives  $\Lambda_F = 24.66^\circ$  and an equatorial disturbance that reaches down to an altitude of 1343 km. Hence, both the 2024 May and the 1872 February events provide evidence of causal disturbance exceedingly close to the Earth.

Table 4 list all 54 sites at which aurora was reliably reported on 1872 February 4 that are at  $\Lambda_M \leq 31^\circ$ . The table shows that there are considerable numbers of sightings at the longitudes of the Middle East and Arabia, at somewhat higher (but still low) latitudes. However, the lowest three  $\Lambda_M$  values (from Gondokoro and Khartoum in Sudan and Aden in the Yemen) are so low, the discussion given above means that we need to treat them with a considerable degree of scepticism. Opinions differ: Silverman (2008) argues that all three are misinterpretations of cable disruption reports; whereas Hayakawa et al. (2023c) agree that the Aden and Gondokoro reports are unsafe but have found the original paper by Pictet (1872) who saw the (red) aurora from Cairo ( $\Lambda_M = 22.09^\circ$ ) and received a telegram there from Khartoum ( $\Lambda_M = 5.85^\circ$ ) asking what the red glow on the northern horizon was. We here include this report, which is from the lowest magnetic latitude in the entire data set but only  $3.86^\circ$  equatorward of Mumbai from where there were at least nine credible observations. On the Gondokoro observation, note that the gufm1 model places this site in the southern geomagnetic hemisphere, but the report states the aurora was to the north. In principle, one could, for a very low source reaching down into the equatorial topside ionosphere, see high-altitude aurora at low elevations from the opposite magnetic hemisphere, but we would expect to see conjugate aurora (Reed & Blamont 1974; Martinis et al. 2018) to greater elevations to the south. We also note that gufm1 is an average model of the main field, and the disturbance to the field may possibly have caused Gondokoro to be in the Northern hemisphere. However, the most likely explanation is that this was not a valid report.

Table 4 shows that although the extremely low latitude sightings during the 1872 February event were mainly in the Indian/Pakistan subcontinent and in the Middle-East/Arabia sectors, there is a global range of longitudes  $\phi_G$  between  $-101.0^\circ$  (San Luis Potosí, Mexico) and  $104.5^\circ$  (Mito, Japan).

The furthest poleward sighting during the 1872 February event was at Polaris Bay, Greenland from the expedition ship ‘Polaris’ ( $\Lambda_G = 81.36^\circ$  N,  $\phi_G = 62.15^\circ$  E, at that date  $\Lambda_M = 73.44^\circ$ ). Interestingly, the aurora even at that high latitude was described as a brilliant red, which was the dominant description all over the globe (Silverman 2008).

Table 5 is the same as Table 4 for the 2024 May event. In this case, observations on 2024 May 10 and 11 are included. Comparison shows that not only does the 2024 May event not reach such low latitudes as the 1872 February event, but also the number of observations below the threshold magnetic latitude is very much lower. There is one, unconfirmed, report on May 11 from Dawwah on Masirah Island off the south-east coast of Oman at  $\Lambda_M = 15.51^\circ$ , which, if confirmed, would lift the May 11 event to second in the ranked list in Table 2. However, no details nor image are available to help confirm the report. On the other hand, the two reports to the west of Muscat have been confirmed and the one at Jabal al Sarat, in the Al Hajar al Gharbi Starlight Reserve, was made by the Oman Astronomical Society and Elizabeth McDonald of NASA/Goddard (the founder of Aurorasaurus project) has confirmed it as an auroral sighting. We

**Table 4.** Locations from where aurora was observed with QD latitude  $\Lambda_M$  below the  $31^\circ$  threshold from where aurora was observed on 1872 February 4 ranked by increasing  $\Lambda_M$  value. The geographic coordinates of the sites are ( $\Lambda_G, \phi_G$ ). Of the 56 low-latitude observations listed (including those in Yemen and the Sudan), 32 came from the Silverman collection, 21 from the papers Hayakawa et al. (2018a) and Hayakawa et al. (2023c) and 3 from Vázquez et al. (2016).

#	$\Lambda_G$ ( $^\circ$ N)	$\phi_G$ ( $^\circ$ E)	$\Lambda_M$ ( $^\circ$ N)	Location name
–	4.90	31.67	–5.58	Gondokoro, Sudan
–	12.81	45.03	2.34	Aden, Yemen
1	15.58	32.53	5.85	Khartoum, Sudan
2	19.12	72.87	9.71	Mumbai, India (Bombay)
3	18.86	82.57	10.11	Jeypore, India
4	21.39	39.86	11.86	Al-Moabdhah, Makkah (Mecca)
5	21.76	72.15	12.52	Bhavnagar, India
6	24.09	32.9	15.25	Aswan, Egypt (Syene)
7	25.65	57.79	16.28	Bandar-e-Jask, Iran
8	25.45	81.85	17.07	Allahabad, India
9	26.86	80.94	18.52	Lucknow, India
10	27.72	68.82	18.78	Sukkur, Pakistan (Aror or Bakhar)
11	27.04	88.26	19.26	Darjeeling, India
12	28.28	68.44	19.37	Jacobabad, Pakistan
13	30.17	71.47	21.53	Multan, Pakistan
14	29.97	32.55	21.84	Suez, Egypt
15	30.05	31.24	22.05	Cairo, Egypt
16	31.22	29.95	23.48	Alexandria, Egypt
17	32.69	51.69	23.95	Ispahan, Iran
18	32.37	75.60	24.08	Madhopore, India
19	30.00	120.58	24.08	Shaoxing, Zhejiang, China
20	11.22	–60.78	24.09	Courland Bay, Tobago
21	32.94	73.72	24.61	Jhelum, Pakistan
22	32.68	35.60	24.62	Masada, Israel (Sebbeh)
23	33.56	73.04	25.24	Rawalpindi, Pakistan
24	31.23	121.49	25.30	Shanghai, China
25	32.19	111.55	26.14	Shengkangzhen, Hebei, China
26	32.38	111.68	26.36	Laohekou, Xiangyang, Hubei, China
27	35.49	74.59	27.38	Raikot, Pakistan (Raikote)
28	33.63	130.23	27.54	Kota, Fukuoka, Japan
29	33.97	135.12	27.74	Yura, Wakayama, Japan
30	33.87	130.65	27.76	Onga, Fukuoka, Japan
31	34.27	133.03	28.09	Imabari, Ehime, Japan
32	34.27	108.95	28.16	Xincheng, XiAn, Shaanxi, China
33	22.16	–100.97	28.35	San Luis Potosí, Mexico
34	34.72	137.73	28.42	Hamamatsu, Shizuoka, Japan
35	34.67	131.85	28.51	Masuda, Shimane, Japan
36	34.83	136.87	28.55	Tokoname, Aichi, Japan
37	34.90	132.10	28.73	Hamada, Japan
38	35.00	135.75	28.74	Kyoto, Japan
39	34.75	113.68	28.78	Zhengzhou, Henan, China
40	35.18	136.90	28.89	Nagoya, Japan
41	35.15	132.40	28.97	Oda, Shimane, Japan
42	35.37	132.75	29.18	Izumo, Shimane, Japan
43	35.68	139.75	29.32	Chiyoda City, Tokyo, Japan
44	35.53	129.33	29.43	Ulsan, South Korea
45	35.95	139.7	29.59	Saitama, Japan
46	18.47	–69.95	29.83	Santo Domingo, Dominican R.
47	36.32	139.80	29.94	Oyama, Japan
48	36.37	140.47	29.98	Mito, Ibaraki, Japan
49	36.38	139.73	30.01	Tochigi, Japan
50	36.25	111.68	30.24	Linfen, Shanxi, China
51	36.65	128.45	30.56	Yecheon-gun, South Korea
52	37.03	140.38	30.64	Tanagura, Fukushima, Japan
53	37.05	140.88	30.65	Iwaki, Fukushima, Japan
54	35.84	14.54	30.96	Marsaxlokk, Malta

**Table 5.** Locations from where aurora was observed with QD latitude  $\Lambda_M$  below the  $31^\circ$  threshold on 2024 May 10 and 11, ranked by increasing  $\Lambda_M$  value. The geographic coordinates of the sites are ( $\Lambda_G, \phi_G$ ). The Class column gives the classification of the observation report: U: unknown – the observer does not record if the observation was by camera or by the naked eye; B: Both – the observer records that the aurora was seen both by camera and by naked eye; VO: Visual Only – the observer records that he/she only made naked-eye observations of the aurora; CNV: Camera but No Visual – the observer records he/she saw the aurora using a camera and specifically states that he/she could not see it by naked eye; CVU: Camera Visual Unknown – the observer reports a camera observation (often by presenting the image) but says nothing about its visibility by naked eye; CAV: Camera-Assisted Visual – the observer reports a camera observation and that although the aurora could be seen by naked eye, it was only found after detecting it by camera.

#	$\Lambda_G$ ( $^\circ$ N)	$\phi_G$ ( $^\circ$ E)	$\Lambda_M$ ( $^\circ$ N)	Class	Location name
1	22.92	57.53	18.08	CVU	Ad-Dāhiliyah, Oman
2	23.32	57.13	18.51	CVU	Jabal al Sarat, Oman
3	27.88	−15.72	18.58	CVU	Mogán, Las Palmas, Gran Canaria
4	27.99	−15.57	18.70	CVU	Cueva Grande, Gran Canaria
5	27.96	−15.57	18.46	CVU	Pico de las Nieves, Gran Canaria
6	28.27	−16.64	19.12	CVU	El Teide, Tenerife
7	19.07	−155.58	19.49	B	NāʻĀlehu, Big Island, Hawaii
8	28.66	−17.81	19.70	CAV	Breña Alta, Santa Cruz de La Palma
9	28.76	−17.88	19.83	CVU	Roque de Los Muchachos Observatory, La Palma
10	28.78	−17.96	19.86	B	Astronorte Observatory, La Palma
11	20.92	−156.38	21.09	U	Kuau beach, Maui, Hawaii
12	14.56	−90.73	24.48	U	Antigua, Guatemala
13	14.72	−90.65	24.65	CNV	San Juan Sacatepéquez, Guatemala
14	32.73	−16.93	24.76	B	Picodo Arierio, Madeira Island
15	18.41	−66.22	24.85	U	Candelaria, Puerto Rico
16	18.09	−67.12	24.89	CVU	Monte Grande, Puerto Rico
17	19.18	−98.64	28.05	U	Iztaccihuatl, Puebla, Mexico
18	32.79	79.00	28.32	B	Hanle, India
19	19.09	−96.14	28.33	B	Heroica Veracruz, Mexico
20	35.85	137.70	29.04	B	Kiso, Nagano, Japan
21	19.29	−81.35	29.24	U	Grand Harbour, Cayman Islands
22	19.30	−81.38	29.25	CVU	Georgetown, Cayman Islands
23	36.10	138.49	29.26	CNV	Koumi, Nagano, Japan
24	36.74	5.05	29.48	B	Bejaia, Algeria
25	36.87	6.92	29.72	CVU	Skikda state, Algeria
26	34.14	77.56	29.81	B	Ley, India
27	34.01	58.17	29.98	CVU	Ferdows, South Khorasan, Iran
28	37.03	14.70	30.36	B	Chiaromonte Gulfi, Ragusa, Sicily
29	37.31	137.15	30.61	B	Noto, Ishikawa, Japan
23	20.73	−89.00	30.68	CVU	Yucatán, Mexico (10 May)
24	20.73	−89.00	30.68	CVU	Yucatán, Mexico (11 May)
25	37.38	136.91	30.70	B	Wajima, Ishikawa, Japan
26	37.65	140.02	30.79	CVU	Kitakata, Fukushima, Japan
28	38.01	−1.49	30.90	U	Murcia, Spain
26	23.25	−106.41	30.91	CVU	Mazatlán, Sinaloa, Mexico
27	22.65	−100.61	30.92	B	Peyote, San Luis Potosí, Mexico
28	38.37	−7.51	31.00	B	Alqueva, Portugal

also note that the online catalogue by C. Wilson (not used here) includes a sighting from Calabarzon, Philippines, which is almost on the Q-D geomagnetic equator. No details are given and this is not included in the present study as it is more than  $10^\circ$  in  $\Lambda_M$  from any other observation.

Table 4 also assigns one of the seven observation classes to each observation report. This is because understanding the role of the camera and of social media on the recent data is more complex than just separating the observations as ‘by camera’ and ‘by eye’. On social media, many observers post images with little more information than the date, time and location. A few state explicitly that if the aurora was, or was not, visible by eye but most do not. Thus,

it is not true to say that if the report does not state that aurora was seen by eye, then it was not seen by eye. Furthermore, as discussed in Section 2, a report that states aurora was not seen by naked eye does not mean that it could not have been seen by naked eye, unless the observer also records that he/she had been in fully dark conditions for the previous hour. However, this last qualification is never fully reported. The seven-fold classification scheme covers all the potential combinations of known circumstances for the low-latitude data. It is laborious to compile and has only been given for the 28 observations in Table 5: there would be years of work in compiling it for the full data set. As discussed in Section 2, information on the level of dark adaptation of the eye makes this information of very limited



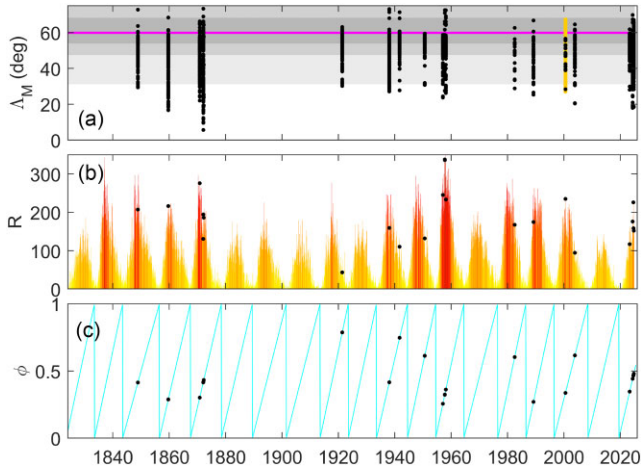


**Figure 14.** Analysis of extreme auroral events in which aurora extends to geomagnetic latitudes below the  $\Delta_M = 31^\circ$  threshold (that is defined in Fig. 11) for 1820 January to 2024 June. **A** the black points show the  $\Delta_M$  of area-combined samples on days classed as extreme events. The bars of different shades of grey and the mauve line give the distribution and mean of  $\Delta_M$  for all samples in the data base, using the same format as in Figs. 13 and 2. The orange bar for the ‘Bastille Day’ event of 2000 July 14 gives the range of  $\Delta_M$  derived from global auroral images from UV imager on the Polar spacecraft, which is used because cloud cover and the timing of the event combined to give fewer ground-based observations of aurora in this event at the lowest  $\Delta_M$ . **B** CR means of sunspot number,  $R$ , in the same format as Fig. 8B. The black points are the values for the CR containing the extreme event. **C** The solar cycle phase variation,  $\phi$ , with the black points marking the extreme events.

value and separation into ‘camera’ and ‘eye’ observations, as done by Hayakawa et al. (2025), is essentially meaningless without proper information on the level of dark attuning of the eye and on the ISO rating of the camera. In this paper, this information is not used in any way and is included in Table 5 just in case it is useful to a future author for a reason other than absolute sensitivity, (for example, colour sensitivity).

#### 4.6 Events that meet the 31-deg threshold

Fig. 14 A plots all the area-combined samples on the dates of events 1–21 in Table 2. These are plotted as a function of date on top of horizontal bars of different shades of grey and a mauve line that give the distribution and mean of  $\Delta_M$  for all samples in the data base, using the same format as in Fig. 2A. The orange bar shows the maximum extent of the mid-night auroral oval seen by the UV imager on the Polar satellite during the Bastille-day storm, and the lack of black points emphasizes the paucity of ground-based observations for this event. Panel B gives the Carrington rotation (CR) means of the sunspot number,  $R$ , using the same coloured bar-chart format as Part B of Fig. 8. Panel C shows the solar cycle phase,  $\phi$ . In parts B and C the black dots mark the date of the events. The plot confirms that events are generally near the peak of the sunspot cycle, although the 1921 and 1941 events are more in the middle of the declining phase. The 1921 event was at a considerably lower sunspot number than any other event. The plot shows that neither large sunspot numbers nor cycle maximum guarantee an event.

The top panel of Fig. 15 is the same as that in 14 and panel C compares it to CR means of the mid-latitude  $aa_H$  geomagnetic index. This shows that the events defined in Table 2 are always accompanied by a geomagnetic storm of considerable magnitude.

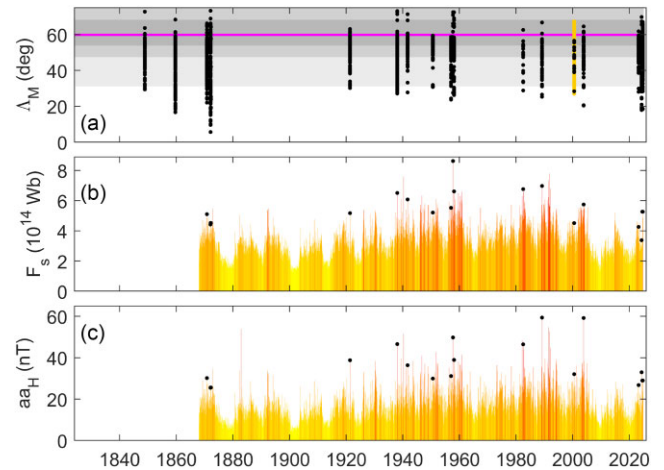


**Figure 15.** **A.** The same as Fig. 14A. **B** is the same as Panel B of Fig. 14 but for CR means of the homogeneous  $aa_H$  index (Lockwood et al. 2018a, b). **C.** the same as part B but for the signed open solar flux  $F_S$  (Lockwood & Owens 2024). The events all occur during CRs when  $F_S$  exceeds  $4 \times 10^{14}$  Wb, but there are a great many CRs when  $F_S$  exceeds this value but no extreme event occurs at Earth.

However, some very large geomagnetic storms are not accompanied by a large global auroral event. The relationship of the auroral events to the geomagnetic storms will be the subject of a later paper.

Lastly, Panel B of Fig. 15 shows CR means of the signed open solar flux,  $F_S$ , as generated by Lockwood & Owens (2024). These are estimated using four geomagnetic activity indices (including  $aa_H$ ) and the algorithm used is calibrated using the modern satellite  $F_S$  estimates by Frost et al. (2022) who used strahl electrons and the method developed by Owens et al. (2017b) to allow for the ‘excess flux’ caused by inversions of the open field lines in the heliosphere (now often called ‘switchbacks’) (Lockwood, Owens & Rouillard 2009a, b). Comparing with Fig. 14B, it is noticeable that high open solar flux is a more important criterion for an extreme auroral event than high sunspot number. In the interval for which we have CR means of  $F_S$  (1868–2024.5) all 17 CRs in which an extreme auroral event occurred had a mean  $F_S$  that exceeded  $4 \times 10^{14}$  Wb; however, there were 476 CRs in which this threshold was exceeded but no extreme event is seen, so only 3.6 per cent of CRs exceeding this  $F_S$  threshold gave an auroral event. Hence, exceeding this threshold in open solar flux is a necessary, but far from sufficient, condition.

#### 4.7 The effects of modern technology

As mentioned above, a number of changes lead us to expect that observations of aurora will be more numerous today than in the past. The biggest factors are the increase in camera sensitivity (and the massively increased availability of such technology because of ‘smart’ mobile phones) and the advent of social media and citizen science internet sites that allow observations from all over the globe to be distributed. In addition, we have improved forecasting of events (and dissemination of those forecasts) to encourage potential observers to seek out dark skies, increased public awareness and higher population densities. There is an important point to make here: some (but not many) modern observers report that they could see the aurora with their naked eye; however, that is not the important question for comparison with older data, which is ‘would they have noted the aurora without the aid of a modern camera and would they have reported it without the internet’: this is a question that

has not been addressed and is not easy to assess. Hayakawa et al. (2025) studied the 2024 May event, sorting the aurora into ‘camera’ and ‘naked-eye’ observations, and find the lowest-latitude confirmed naked-eye observations on 2024 May 10/11 were from El Peyote and Hanle, India (QD latitudes,  $[\Lambda_M]$  of  $31.28^\circ$  and  $27.97^\circ$ , respectively). However, we have found some lower-latitude reports and some specifically state that the aurora was observed by eye as well as photographed: the lowest latitude of these is that mentioned above in Section 3.1 and reported by Brenda Trowbridge in Naalehu, Hawaii ( $\Lambda_M$  of  $19.50^\circ$ ) and a naked eye report and photograph from Breña Alta, Santa Cruz de La Palma ( $\Lambda_M$  of  $19.70^\circ$ ), both of which are equatorward of El Peyote and Hanle. Hence, the 2024 May event classifies as an extreme event by our criteria for both naked-eye and camera observations. In addition, Hayakawa et al. (2025) note reports from Oman but as they were, at that time, of unknown provenance, attributed the lowest Northern-hemisphere camera observations to San Juan Sacatepéquez in Guatemala ( $\Lambda_M$  of  $24.65^\circ$ ). Subsequently, photographic evidence from two locations in Oman have appeared on the internet, one being the image by Yahya Al Kindi of the Oman Astronomical Society that was sent to, and confirmed by, Elizabeth McDonald at NASA/Goddard. It is not clear if the second sighting from Ad-Dāhiliyah, reported via Aurorasaurus, is independent of that from Jabal Al Sarat (there is a different image) but at  $\Lambda_M$  of  $18.08^\circ$  and  $18.51^\circ$  these are the lowest magnetic latitude observations of aurora during the 2024 May event.

We believe there are two major problems with simply using the criteria of observation by eye and by camera distinction when trying to evaluate a modern auroral event against past events. The first reason is that most citizen reports are now made by posting a digital image on the internet and only in very rare cases do they report if they could, or could not, see the aurora by naked eye. Even then, there is an important difference between spotting the aurora by eye and then taking a photograph of it (which is equivalent to a historic sighting) and using a camera to find the aurora and then looking to see if you can also see it with the naked eye (which is not). However, the larger problem is our lack of knowledge of the dark-adaptation of the eye which, as shown in Section 2 makes the difference between the camera being more sensitive than the eye and the reverse. In this paper, we are comparing the lowest-latitude observations, which will be of lower intensity and close to the northern horizon. These circumstances will tend to select observations by observers with optimally dark-attuned eyes and Section 2 shows that such eyes are similar in their sensitivity to even SLR digital cameras. Hence, for the purposes of our ranking of events by the lowest latitude of observation, the increased use of digital cameras in the 2024 May event is not a significant factor.

If we reject observations that are reported as being by camera (the CVU classification in Table 5) as being the same as those that specifically state the aurora was not visible by eye (the CNV classification) we eliminate the majority of modern sightings, and this will reduce both the numbers and latitudinal extent of events that we derive. We have demonstrated for the 2024 May events, that if we treat all CVU classified observations as being actually CNV (i.e. we only classify as by camera, by eye or both), then the lowest magnetic latitude is increased by  $0.58^\circ$  for May 10 and by  $1.41^\circ$  for May 11. However, because at least some CVU reports could be B classifications (both by camera and eye) in reality and so not CNV, these increases in the lowest magnetic latitude must be considered as overestimates. Hence, the drop in ranking for May 11 if we only allow naked-eye reports (from 3 to 5) is almost certainly excessive (that for May 10 is unchanged). Because a number of factors have changed, we need a more holistic approach to compare the May events with

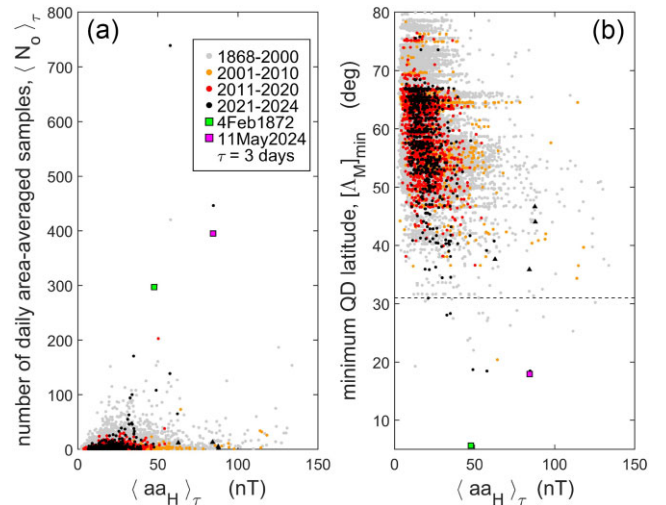


**Figure 16.** Comparisons of **A** the number of area-combined auroral observations samples on a given night,  $N_o$  and **B** the minimum QD geomagnetic latitude,  $[\Lambda_M]_{\min}$  on a given night, both with the  $aa_H$  geomagnetic activity index for that date. Three-day running mean smooth has been applied to the  $aa_H$  data (the averaging period,  $\tau = 3$  days). The grey points are for 1868 (the start of the  $aa_H$  data) to 2000, inclusive; the orange points for 2001–2010; the red points for 2011–2020 and the black points for 2020–2024. Later points are plotted after (and so on top of) earlier ones. The four black triangles are examples in the post 2020 data when  $\langle aa_H \rangle_\tau$  is high (above 60 nT) but  $N_o$  is low (below 15). The green and mauve squares are for the 1872 February 4 event and for the 2024 May 11 event, respectively.

past events and not just focus on the camera or eye distinction (about which we anyway have inadequate information in most cases).

Fig. 16 provides a first attempt at looking at the combined effects of all the changes generated by the availability of smartphone cameras and the internet, by comparing the relationship with geomagnetic activity level, quantified by the  $aa_H$  index, for different epochs.

To make this comparison, we take 3-day running means of the  $aa_H$  index. We do this for two reasons. Firstly, some auroral records may be a day out because no UT was given for the observation and the ‘astronomical night’ convention was not followed (i.e. observers increased the date by a day at mid-night). Even if the date and time were clearly defined, simultaneous observations of the same aurora made just east and west of the international date line would differ by day. Secondly, the daily  $aa_H$  data in Fig. 16 are averages between 12 UT on one day and 12 UT on the next. This corresponds to the astronomical night for the Greenwich meridian but is 12 h early for the astronomical night just east of the International Date Line and is 12 h late for just west of the International Date Line. The effects of these phasing differences are reduced if 3-day running means are taken. To test this, Fig. 16 was also generated using  $\langle aa_H \rangle_\tau$  intervals that were shifted back and forward by 12 h, and there was no significant change to Fig. 16.

The construction of  $aa_H$  has been aimed at making it as homogeneous as possible so it is a consistent measure throughout the data series Lockwood et al. (2018a, b). However, it is worth noting that, although  $aa_H$  is the best-calibrated index that we have, which extends back into the 19<sup>th</sup> century, it is not perfect. In particular, early in the data series there are data gaps in one or both of the hemispheric data series and the 1872 February event is a good example of this. Near the peak of this event, the geomagnetic data for the Northern-hemisphere (from Greenwich) have data gaps, which causes the daily means (which we use here) of Northern-hemisphere index ( $a_{HN}$ ) to

be smaller than Southern-hemisphere data index ( $aa_{HS}$ ) in this event. We know from the records of Mayaud (1980), who compiled the original  $aa$  index, that the Melbourne data were, unlike Greenwich, continuous during this storm. Using  $(a_{HN} - aa_{HS})/2$  as an error estimate in  $aa_H$ , we find it is roughly 20 per cent during the 1872 February event, which is large for  $aa_H$  but not an outlier. We also note that the overall error performance for daily means of  $aa_H$  is very similar to that of the modern 3-hourly  $am$  index. So the use of one station in each hemisphere for  $aa_H$  effectively costs us a factor 8 in time resolution compared to the  $am$  index that uses 10 to 12 stations in each hemisphere. However  $am$  only extends back to 1959, whereas  $aa_H$  is uniformly calibrated back to 1868.

Part **B** of Fig. 15 shows that events of very low-latitude aurora are almost always accompanied by high  $aa_H$ , averaged over the CR,  $\langle aa_H \rangle_{CR}$ ; however, not all events of high  $\langle aa_H \rangle_{CR}$  are accompanied by a low-latitude auroral event. Hence, from this, we expect there to be some anticorrelation between the minimum geomagnetic (QD) latitude on a given night,  $[\Lambda_M]_{min}$  and the  $aa_H$  index, but it may not be a high one. Part **B** of Fig. 16 confirms that this is the case. By using different colours for different epochs, this plot studies how this relationship has changed over time. The average behaviour of  $[\Lambda_M]_{min}$  over the last 4 yr (the black dots) is not substantially different from earlier epochs; however, the anticorrelation of  $aa_H$  and  $[\Lambda_M]_{min}$  is somewhat stronger for the recent data and there is a clear (non-linear) relationship between them. The spread of points towards the right of the plot (i.e. high  $aa_H$  with only average  $[\Lambda_M]_{min}$ ) is great for the older data, which does imply that low-latitude aurora that were not always seen in earlier years during events of large  $aa_H$ . Some of this will be because of aurora that have been reported in modern data would have been missed in older data. However, the four events shown by small black triangles show that high  $aa_H$  without a great auroral event (i.e. the minimum magnetic latitude is not low and the number of observations is not high) have still occurred in modern data. This indicates that this is due to a limitation to the anticorrelation between geomagnetic activity and minimum geomagnetic latitude of aurora geomagnetic and some strong geomagnetic storms are not accompanied by low-latitude aurora. We must remember that the interval of the modern data (2021–now, inclusive) is shorter by a factor of 38 than the pre-millennium interval (1868–2000, inclusive) making the number of these such occurrences in the modern data correspondingly smaller. The horizontal dashed line in Fig. 16 **B** is the 31-deg threshold for extreme events adopted here, and the Figure shows that there is no significant difference in the spread of  $aa_H$  values at which extreme events ( $\Lambda_M < 31^\circ$ ) occurred between the modern data or earlier data. This strongly implies the detectability and reporting of low-latitude aurora has not increased. For example, the event of 2024 May 10 took place at a very similar  $aa_H$  to that during the event of 1872 February and yet aurora was seen to a lower latitude in the 1872 event than in the 2024 event. We conclude there is no evidence in this analysis that the minimum (geomagnetic) latitude extent of aurora in the extreme event has increased in recent years, although the full extent of some events are likely to have been missed in the past (particularly for geomagnetic storms in which  $aa_H$  exceeds 100 nT), compared to what would be detected today. We note that Love et al. (2025) use superstorms in the years between 1859 and 2005 and find a coherent variation of low-latitude extent with observed or estimated peak geomagnetic  $Dst$  disturbance, independent of the use of camera or naked eye observations. Hence, this work also finds no evidence that the use of caneras in modern times has increased the low-latitude extent of aurorae.

In contrast, 16A presents the same study for the total number of observations on a given night,  $N_o$ . The recent data (black points)

increase with  $aa_H$  more steeply than for the older data, so that the black dots sit on the upper envelope set by the historic data. We note there is actually less reporting of quiet-time aurora compared to the historic data but greater reporting of larger events: it seems that humans, collectively, are now less interested in monitoring the aurora at all disturbance levels but more interested in observing large events.

We conclude that recent advances in forecasting, observing and recording of auroral observations have greatly increased the number of observations for a given size of large event, as quantified by geomagnetic activity. However, the evidence also strongly suggests that this has not greatly increased the latitudinal spread over which observations have been made during extreme events.

The auroral intensity decays with latitude at the low-latitude boundary of a great aurora. However, it is possible that this is limited to the lowest one degree of magnetic latitude in great auroral events. Shiokawa et al. (1996) and Vichare et al. (2024) have shown that at the peak of a major low-latitude auroral event, there is an enhancement in the BBE flux responsible for exciting the low latitude aurora. This lies very close to the equatorward edge of the precipitation. Hence, the effect of enhanced detectability granted by digital cameras over un-attuned human eyes will be smaller at the equatorward edge of the aurora than at higher latitudes between the main auroral oval and this enhanced BBE feature at the low-latitude rim of the aurora. The observations show that the equatorward edge of this enhanced BBE is a sharp gradient, with the BBE flux decaying over about one degree of geomagnetic latitude. This is true at all energies of the BBE but particularly for the lowest energies that generate aurora at the greatest heights that is detectable over the horizon from the lowest latitude sites. Hence, the effect of observer sensitivity (camera or naked eye) on the lowest latitudes may be limited to only one degree, which offers another explanation of the lack of change in Fig. 16 b in the occurrence of extreme low-latitude auroral events.

There is one remarkable point to note about the observations from Oman in the 2024 May event. From most low-latitude locations, such as Central America, the Canary Islands and Japan, the low-latitude aurora was red and so from high altitudes, allowing a large latitudinal separation between the geomagnetic latitude of the precipitation and the observer. The images from both Ad-Dāhiliyah and Jabal al Sarat in Oman clearly show green, as well as red, aurora. This shows that the BBE feature on the low-latitude edge of the aurora extended up to kilovolt energies at this time. This implies that the separation between the Oman observers and the precipitation field line was smaller in this case because of the lower altitude of green emission.

We note that some of the scatter in Fig. 16 b at the lowest latitudes might be reduced if we applied accurate corrections for the offset in geomagnetic latitude of the observed and the field line of the causal precipitation. Given we have images for most modern reports, which means from the colour we can estimate the altitude of emission, we could do this for the modern data. This will be the subject of a later publication.

#### 4.8 Relationship to solar active regions

Fig. 14 **B** shows that, although none of these extreme auroral events occur at sunspot minimum, they do not require an especially high sunspot number. This point is emphasized by the ‘Halloween’ events of 2003 October/November that was followed by the 2003 November 20 extreme auroral event. This interval is shown in Fig. 17, in the same format as Fig. 2. Note that comparison of Panel **A** of Figs 2 and 17 reflects how much internet reporting of auroras grew between 2003 and 2015.



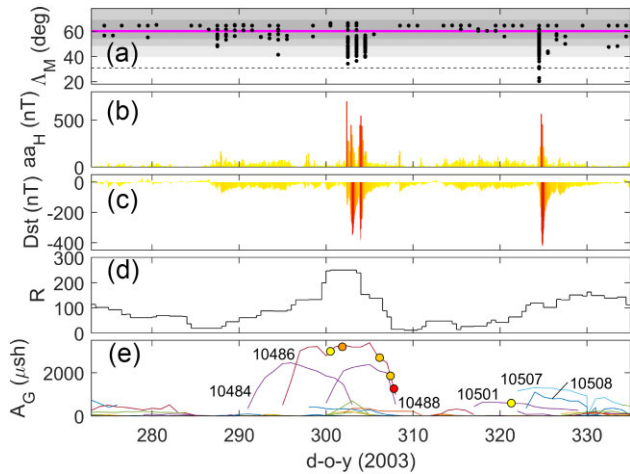


**Figure 17.** Analysis of the ‘Halloween’ events of 2003 October/November, followed by the 2003 November 20 extreme auroral event. The format is the same as Fig. 2. In part **E** the numbers are the numbers of the sunspot groups labelled in Fig. 18 and yellow dots denote the occurrence of an M-class flare in that sunspot group and orange and red points denote X-class flares, the red point being the largest flare ever recorded. The horizontal dashed line in **A** is the  $31^\circ$  threshold of  $\Lambda_M$  used in this paper to define extreme auroral events.

The series of events referred to as the ‘Halloween Storms’ began on October 29 and on three successive nights aurora was seen at unusually low latitudes. However, the lowest magnetic latitude reached was only  $\Lambda_M = 34.34^\circ$  and so these nights do not meet the  $\Lambda_M = 31^\circ$  threshold that we have set to define extreme events. Fig. 17 shows that just 22 d after the onset of the first Halloween storm (i.e. significantly less than a full CR period), there was another event on November 20 that does meet our threshold and in which the geomagnetic disturbance in both the  $aa_H$  and the  $Dst$  indices (panels **B** and **C**, respectively) was larger than seen in the events of October 29–31. This is despite the fact that the sunspot number, shown in panel **D**, was considerably lower than it had been during the Halloween storms.

Panel **E** of Fig. 17 shows that there was a rapid rise in group area, particularly group 10486, before the October 29–31 (Halloween) events, but the groups were of much more modest area before the November 20 event. Hence, these events demonstrate that neither sunspot number nor the size of sunspot groups is a good predictor of the size of subsequent auroral and geomagnetic disturbances. In fact, the CME and associated flare that gave rise to the 2003 November 20 storm was in group 10501 (Srivastava et al. 2009), which was not even the largest group on the disc at the time and was very small compared to the group 10486, which produced multiple X-class flares.

Parts **C** and **F** of Fig. 18 compare the solar disc the day before, respectively, the first Halloween storm and the November 20 storm. The first Halloween storm was associated with an X17 flare in sunspot group 10486 on October 28, when it was close to the central meridian as shown in part **C**: this group was responsible for a series of flares and subsequently generated an X2, an X3 and a massive X28e (estimated) flare when close to the western limb, shortly before rotating off the visible disc. On the other hand, part **F** shows the much smaller group at the centre of the disc that was responsible for the November 20 storm. The inserts show detailed views of the two groups. The key point is that the group causing the Halloween storms was much larger in area and generated more and larger flares, but the November 20 storm was larger in both auroral area and geomagnetic disturbance. This case illustrates that sunspot group area is not a

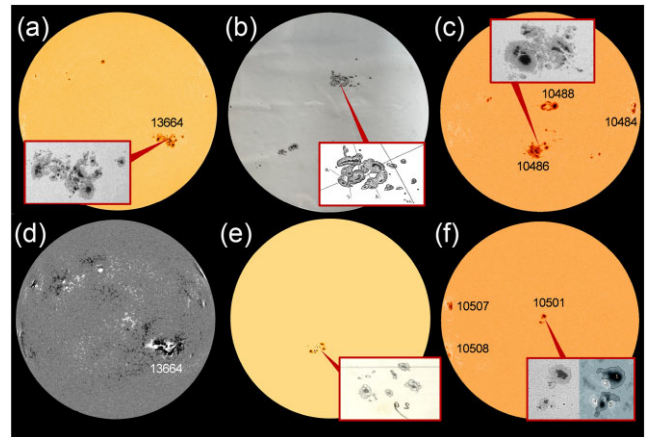


**Figure 18.** Active region sunspot groups associated with events ranked 1, 3, 4, 5, and 6 in Table 2. Sunspot groups are labelled with the AR numbers assigned by NOAA. **A**, Continuum image of the Solar disc made by the HMI (Helioseismic and Magnetic Imager) instrument on Solar Dynamics Observatory on 2024 May 10 showing sunspot group 13664 (shown in greater detail in the inset): Part **D**, beneath **A**, shows the magnetogram taken simultaneously by the same instrument. **B** Richard Carrington’s sunspot group drawings for 1 September 1859: the whole disk is from RAS MS Carrington 3, v. 2, f. 313a (reproduced courtesy the Royal Astronomical Society of London) and the close up detail is from his paper in Monthly Notices (Carrington 1859). **E**, beneath **B**, shows a reconstruction of the sunspot group near the centre of the solar disc that is thought to have given rise to the storm of 1872 February 4: this is drawn from the solar drawings for 1872 February 3 by Angelo Secchi and Louis Bernaerts and contains only the common elements of those two drawings: the inset shows the sketch by Secchi (from Hayakawa et al. 2023c). **C** Continuum image of the Solar disc made by the MDI (Michelson Doppler Imager) instrument on SoHO (Solar and Heliospheric Observatory) satellite on 2003 October 29 showing sunspot group 10484 (shown in greater detail in the inset): Part **F** beneath **C** shows the solar disc 22 d later seen by the same instrument on 20 November 2003 with just one central group (10501): the inset shows the active region and a magnetogram plot, revealing the magnetic structure (Oreshina, Oreshina & Somov 2012).

good predictor of the storm amplitude. This raises two possibilities. Firstly, it may be that big sunspot groups can untangle complex field structures with many small releases of energy and material and hence without the release of a large CME. Alternatively, the internal structure in a CMEs released by a big sunspot group may be more complex. The latter possibility could have two effects: firstly the geoeffectiveness of a CME could depend on which part of it impacts Earth’s magnetosphere (c.f. Owens, Lockwood & Barnard 2017a); secondly the field at Earth might vary more and so there is no prolonged interval of strongly southward IMF that gives sustained transfer of solar wind energy into the magnetosphere.

Because the 2024 May 10 event was associated with an exceptionally large sunspot group (see parts **A** and **D** of Fig. 18) as, famously, was the Carrington event (see part **B**), there is a widespread belief that these events are always generated by exceptionally large sunspot groups and that exceptionally large sunspot groups always drive great auroral events. Neither of these two assumptions is correct. The point is illustrated by Fig. 18E, which is a reconstruction of the solar disc, showing the group that generated the greatest known auroral event, that of 1872 February 4, a group that was not at all exceptional in area.

Table 6 and Fig. 19 demonstrate the lack of a consistent relationship between source sunspot group area and the extent of the auroral event. Columns 7, 9, and 11 show where a given value sits

**Table 6.** Areas of sunspot groups identified as the origin of CMEs that generated the 21 extreme auroral events listed in Table 2 compared with the effects of the 21 largest sunspot groups by area (note that the 1989 March 13 and the Fátima storm of 1938 January 25 fall into both these categories), plus the St Patrick’s Day storm studied in Fig. 2. For the 21 large-area spot group cases, the peak disturbance (minimum  $\Lambda_M$ , maximum  $aa_H$  and minimum  $Dcx$ ) is taken for the interval between the large group first appearing and one day after (to account for propagation time to Earth) it has rotated off the disc. Note also that group 12673, which peaked in area at 3267  $\mu sh$  on 1938 January 21, generated two geomagnetic/auroral storms. The second of these was the larger and is the Fátima Storm, ranked number 13 in the list of exceptional storms listed in Table 2: this was caused by a CME launched just before the group rotated off the east limb of the Sun. The areas given are the maximum whole spot group area (in millionths of a solar hemisphere) attained by the group in question. The rank number (available down to #24) is by the peak area of the sunspot group (Meadows 2024). Note that the values for 1859 August 28 are uncertain, as the associated flare has not been unambiguously identified. References giving the group area are: a. Meadows (2024); b. Hayakawa et al. (2021); c. Debrecen Photoheliographic Database; d. Hayakawa et al. (2025); e. Love & Coisson (2016); f. Ishkov (2016) (English translation available from ResearchGate); g. Love et al. (2019a); h. Hayakawa et al. (2023c); i. Silverman (1995); j. Hayakawa et al. (2023b).

1	2	3	4	5	6	7	8	9	10	11
Event date	Group number	Group area ( $\mu sh$ )	area rank	ref	minimum $\Lambda_M$ ( $^\circ$ )	$P_{LT}(\Lambda_M)$ (per cent)	minimum $Dcx$ (nT)	$P_{LT}(Dcx)$ (per cent)	maximum $aa_H$ (nT)	$P_{GT}(aa_H)$ (per cent)
1947-Apr–8	14886	6132	1	a,c	46.7	0.7732	−78	1.5816	96	1.0371
1946-Feb–7	14417	5202	2	a,c	39.1	0.1216	−214	0.0755	99	0.0191
1951-May–19	16763	4865	3	a,c	52.0	3.8742	−47	5.4040	41	9.2713
1946-July–29	14585	4720	4	a,c	42.1	0.2934	−246	0.0463	322	0.0356
1947-Mar–12	14851	4554	5	a,c	40.1	0.1471	−195	0.0997	186	0.1600
2014-Oct–24	12192	4419	6	a,c	50.0	1.9919	−50	4.6968	78	1.8719
1989-Mar–13	5395	4201	7	a,c	25.3	0.0095	−564	0	722	0.0007
1990-Nov–16	6368	3827	8	a,c	50.6	2.5039	−143	0.2818	170	0.2006
1926-Jan–19	9861	3716	9	a,c	33.1	0.0588	n.a.	—	343	0.0298
1938-Jan–21	12673	3627	10	a,b,c	31.9	0.0407	−326	0.0110	650	0.0017
				and	26.5	0.0104	−336	0.0090	656	0.0015
1917-Feb–14	7977	3590	11	a,c	48.8	1.3024	n.a.	—	141	0.3399
2003-Oct–30	10486	3338	12	a,c	34.3	0.0683	−372	0.0044	698	0.0011
2001-Mar–29	9393	3387	13	a,c	38.1	0.1021	−380	0.0036	298	0.0432
1938-July–20	12902	3379	14	a,c	57.0	17.355	−125	0.4346	125	0.4734
1937-Oct–5	12553	3340	15	a,c	38.7	0.1106	−171	0.1554	126	0.4626
1905-Feb–2	5441	3339	16	a,c	40.1	1.4081	n.a.	—	155	0.2676
1937-July–28	12455	3303	17	a,c	48.8	1.3024	−165	0.1748	221	0.1024
1937-Apr–26	4474	3274	18	a,c	53.6	6.5206	−91	1.0577	159	0.2462
1991-Mar–23	6555	3257	19	a,c	41.9	0.2461	−281	0.0249	362	0.0249
1989-June–16	5528	3249	20	a,c	45.0	0.5217	−132	0.3675	105	0.7748
1991-Oct–27	6850	3234	21	a,c	38.9	0.1166	−280	0.0256	267	0.0596
1859-Sept–1	C520	2971	24	a,c,j	18.6	0.0044	n.a.	—	n.a.	—
1982-July–13	3804	3092	—	c	28.8	0.0160	−325	0.0113	447	0.0126
2024-May–10	13664	2761	—	d	18.1	0.0023	−390	0.0031	521	0.0070
1941-Sept–18	13937	2598	—	e,c	27.7	0.0130	−404	0.0026	459	0.0112
1859-Aug–28	C520	2300	—	f	16.7	0.0015	n.a.	—	n.a.	—
1921-May–14	9334	1709	—	g	30.2	0.0175	n.a.	—	831	0
2000-July–14	9077	1591	—	c	28.2	0.0142	−295	0.0197	352	0.0247
2015-Mar–15	12297	788	—	c	36.6	0.0848	−215	0.0740	264	0.0622
1909-Sept–25	6728	632	—	i,c	31.0	0.0233	n.a.	—	576	0.0039
1872-Feb–4	S29	627	—	h	9.7	0	n.a.	—	626	0.0022
1950-Aug–19	16588	574	—	c	30.8	0.0222	−260	0.0373	202	0.1320
1957-Jan–21	17829	557	—	c	23.7	0.0073	−255	0.0400	416	0.0169
2003-Nov–20	10501	510	—	c	20.4	0.0058	−418	0.0021	564	0.0050

in the overall distribution of that particular parameter. The auroral data set for 1650–2024.5 covers 136 814 nights. Column 7 gives the percentage,  $P_{LT}(\Lambda_M)$ , of the 136 966 nightly minima of  $\Lambda_M$  that are smaller than the value given in Column 2. Between 1932 and 2015 there are 739 968 definitive hourly values of  $Dcx$  that range between +108 nT and −565 nT and this gives us a reference distribution of  $Dcx$  values to help evaluate the relative magnitudes of the various storms in the ring current: column 8 gives the percentage of the 739 968  $Dcx$  values that are more negative than the minimum value for that storm,  $P_{LT}(Dcx)$ . Between 1868 and 2024.5 there are 457 240 3-hourly values of  $aa_H$  that range between 0.37 nT and 831.52 nT: column 11 of Table 6 gives the percentage of these values that are greater than the corresponding  $aa_H$  value in column 10,

$P_{GT}(aa_H)$ . These percentages quantify how extreme an event was, as detected in the parameter in question. Note that  $P_{LT}(\Lambda_M) = 0$  for the 1872 February 4 event because that is the most equatorward aurora in the record. Similarly,  $P_{LT}(Dcx) = 0$  for the 1989 March 13 event as the lowest recorded  $Dcx$  value was during this storm and  $P_{GT}(aa_H) = 0$  for the 1921 May 14 event as the largest  $aa_H$  value was during that storm. Hence, which storm is found to be the largest depends on which parameter is used to quantify it.

Part A of Fig. 19 shows that there is a strong anticorrelation between the peak of the mid-latitude geomagnetic index  $aa_H$  and the minimum of the (predominantly) ring current index  $Dcx$  ( $r = -0.86$ ), as expected. There is also a good correlation between the minimum geomagnetic latitude of the aurora,  $\Lambda_M$  and the

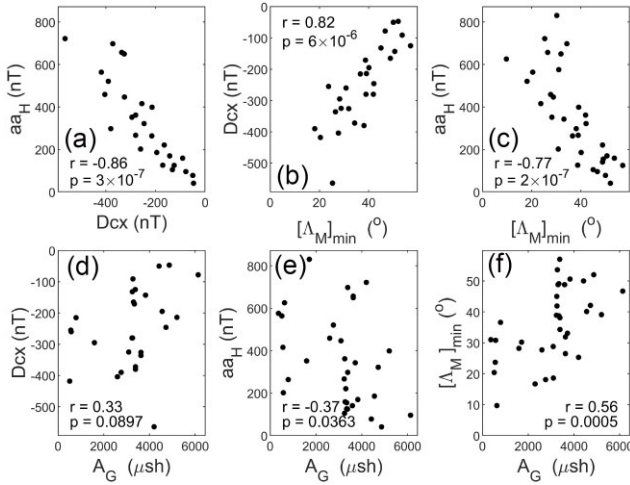


**Figure 19.** Scatter plots of the relationships between the peak geomagnetic disturbances in indices  $Dcx$  and  $aa_H$ , the area of the causal sunspot group,  $A_G$ , and the lowest latitude QD magnetic latitude at which the aurora was seen,  $[\Lambda_M]_{min}$ . In each case, the correlation coefficient  $r$  is given with the  $p$ -value of the null hypothesis that there is no correlation or anticorrelation: values of  $p$  below 0.05 indicate a correlation that is significant at the  $2\sigma$  level. The data set is the list of events given in Table 6.

minimum  $Dcx$  ( $r = 0.82$ , part **B**) and a good, but slightly less strong, anticorrelation with the peak  $aa_H$  ( $r = -0.77$ , part **C**). These correlations are all significant at better than the  $4\sigma$  level ( $p < 1 \times 10^{-4}$ ) and in Parts **A** and **C** they are even significant at the  $5\sigma$  level ( $p < 6 \times 10^{-7}$ ). Hence, auroral event extent is certainly anticorrelated with deep minima in the ring current index  $Dcx$  (as has also been found for the  $Dst$  index by Love et al., 2025) and correlated with strong maxima in mid-latitude geomagnetic indices such as  $aa_H$ .

The bottom row of Fig. 19 looks at the relationship to the area of the causal sunspot group,  $A_G$ . The correlations are weak with the geomagnetic responses and not highly significant (significance levels are only  $1\sigma$  in **D** and **E** but is at the  $3\sigma$  level for **F**). Somewhat surprisingly, the causal group area  $A_G$  anticorrelates with all three terrestrial measures of enhanced activity (i.e. it correlates with the  $Dcx$  and the minimum  $\Lambda_M$  value, and anticorrelates with  $aa_H$ ). Notice, however, the scatter is large and very low latitude aurora can result from a small group (as in the Secchi event) or a very large one (as in the Carrington event).

Cliver, Pötzi & Veronig (2022b) have studied the relationship of the area of sunspot group from which an Earth-bound CME emerges and the magnitude of the geomagnetic storm response. These authors find most storms originate from small groups but that large groups are more likely to generate a large storm: at first sight this appears to be a paradox but is not because small groups are much more common than large ones. They do find that groups of area above  $3500 \mu sh$  are much less likely to generate a large geomagnetic storm. Cliver et al. (2022b) do not study the extent of auroral events but Part **B** of Fig. 16, at least for the more recent data, and parts **B** and **C** of Fig. 19 suggest that their conclusions will apply to great auroral events as well as geomagnetic storms. Hence, parts **D**, **E** and **F** of Fig. 19 appear to be consistent with the (Cliver et al. 2022b) results because respectively, large negative  $Dcx$ , large  $aa_H$  and low  $\Lambda_M$  are all less common if  $A_G$  exceeds about  $3500 \mu sh$ . (Cliver et al. 2022b) argue that this is because the emission of large CMEs is suppressed in large sunspot groups. The size and location of sunspot groups associated

with large terrestrial disturbances has also been studied by Willis, Henwood & Stephenson (2006) and Willis, Henwood & Stephenson (2009).

## 5 CONCLUSIONS

We have presented a survey based on 374.5 yr of auroral observations. Our criteria for defining an extreme auroral event, in terms of how close to the magnetic equator it is observed, generates just 21 nights out of the total of 136 966 nights in the interval: this is an occurrence of just 0.0146 per cent of nights. We use only data from the Northern hemisphere in the interest of making the record as homogeneous as possible. Because of data quality concerns, we restrict detailed attention to after the Dalton minimum. The only nights before the Dalton minimum that meet our criterion are 1768 August 6, 1769 July 19, 1770 September 17, 1784 November 13, and 1789 November 14: of these the only Q-D latitudes reached below  $\Lambda_M = 30^\circ$  are during the 1770 event. This is almost certainly in large part because of the relatively poor observation records in the 17th and 18th centuries; however, the quieter solar conditions are likely to have also contributed. If we take the interval of good observations to be from just before the start of the Dalton minimum to the present day (1790–2024.5), the percentage of nights giving events that meet our criterion rises to 0.023 per cent for this interval there is an average of 2.22 reports per night and aurora is seen, at some location, on 48.04 per cent of nights. These figures exceed those for recent years.

We find that these events are always accompanied by a large geomagnetic storm, but many events of geomagnetic activity at or exceeding this level do not give an auroral event that meets our criteria. The events all occur around the peak of the solar cycle (a few are in the declining phase), but do not correlate well with sunspot number: indeed, both average auroral latitude and the number of extreme events is greater at moderately large sunspot number than at very high sunspot number.

Both nights of the event of 2024 May 10–11 qualify as extreme events, but they only rank as third and sixth in our list of events, ranked by the lowest magnetic latitude reached. The greatest event, by far, is the event of 1872 February 4 in which aurora reached record lows in geomagnetic latitudes all around the globe.

The extreme auroral events do not occur at the minima of solar cycles, but their occurrence is not otherwise controlled by the sunspot number. All these events occur when the open solar flux is very high; however, very high open flux does not guarantee an event will occur.

Looking at the areas of the sunspot groups from which the causal CME emerges, there are a great many very large-area groups that pass across the solar disc without giving a major auroral storm and, although both large and small sunspot groups can give auroral ‘superstorms’, overall there is a slight, but significant, anticorrelation between auroral and geomagnetic responses and the area of the sunspot group from which the responsible CME emerged.

Our ranking the events by low-latitude extent is similar in spirit, but different in detail, to that of Love et al. (2025). We have not made a distinction between camera and naked-eye observations, as was employed by Hayakawa et al. (2025) because the science of the extremely large dynamic range of the human eye tells us that, without quantification of the dark-adaptation of the eye, this has no value nor meaning. We note that there are many examples in the literature where authors report that aurora was observed by camera but not seen by eye; however, this is not something we can draw any proper conclusions from, because in almost all cases we do not know the level of dark adaptation of those eyes, which depends on the local lighting level in the immediate surroundings of the observer and the



behaviour of the observer prior to the observation. A key point is that fully dark-adapted eyes can rival modern cameras in sensitivity, but the comparison does depend on wavelength. By comparison with geomagnetic data, in this paper we find no evidence that the low-latitude extent of aurora has been increased in recent events by modern cameras, which was also true of the study presented by Love et al. (2025).

## ACKNOWLEDGEMENTS

The authors wish to thank many scientists and auroral enthusiasts who contributed dates and places of auroral sightings. Particular thanks go to Sam Silverman, who's extensive catalogues are available from NASA/NSSDC on request. We also thank a number of space weather internet sites that contributed recent sightings, in particular Spaceweather.com for the archive provided by their Auroral Image Gallery. We also thank the citizen science projects Aurorasaurus, AuroraReach, and Skywarden, which we searched for observations of the 2024 May event. We thank a number of data centres: WDC-SILSO, Royal Observatory of Belgium, Brussels for the sunspot numbers used in this paper; the Heliophysical Observatory, Debrecen, Hungary for the Debrecen Photoheliographic Database; The University of Oulu for the *Dcx* index; and the International Service for Geomagnetic Indices (ISGI) for the hemispheric *aa* index data, which we use to generate *aa<sub>H</sub>*. We also thank the VIIRS Imagery and Visualization Team, CIRA, Colorado State University, USA for the whole oval auroral image composites and Will Dunn (WD Photography), Nick Bull (Stonehenge Dronescape), Maximilian-Vlad Teodorescu (Maximus Photography, Romania), Crystal Sibson (Crystal Sibson Photography), and Giovanni Tessicini for the ground-based auroral images. ML and MJO are grateful to the UK Science and Technology Facilities Council (STFC), who part funded this work through grant number ST/V000497/1. The work of WB was supported by the UK Natural Environment Research Council.

## DATA AVAILABILITY

The Supplementary Information file attached to this paper gives all records since the year 2000 with computed QD latitudes. The full data set of auroral observations since 1650 used in this paper is available on request from ML (m.lockwood@reading.ac.uk) but presently is in the form of a variety of files in different formats and the QD latitude for each observation needs to be added (at present it is computed for each auroral report in the software). The data will be published in a homogenized form as soon as we can, with a DOI, but we need to carry out some further work to expunge any surviving duplicates and check the source for each of the 0.2 million records. Much of this work has been completed: until then, the author can provide the data in a series of files with the MATLAB software to read them and add the QD geomagnetic latitudes (which takes of order 15 min to run on the whole data set on a standard laptop). The sunspot data used were generated by WDC-SILSO/SIDAC, Royal Observatory of Belgium, Brussels and are available from <https://www.sidc.be/SILSO/datafiles>. The sunspot group areas are retrieved from the Debrecen Photoheliographic Database <http://fenyi.solarobs.epss.hun-ren.hu/en/databases/DPD/>. The definitive *Dcx* index (at the time of writing, up to the end of 2016) is available from Oulu University at <http://dcx.oulu.fi/?link=queryDefinite> and provisional *Dcx* from <http://dcx.oulu.fi/?link=queryProvisional>. The homogeneous *aa<sub>H</sub>* geomagnetic index is stored in the supplementary information files attached to the papers by Lockwood et al. (2018a) and Lockwood et al. (2018b).

## REFERENCES

- Abbott W., Chapman S., 1959, *J. Atmos. Terr. Phys.*, 14, 111  
 Alken P. et al., 2021, *Earth Planets Space*, 73, 49  
 Allen J., Sauer H., Frank L., Reiff P., 1989, *Eos*, 70, 1479  
 Angot A., 1896, *The Aurora Borealis*. Kegan Paul, Trench, Trubner and Co., London  
 Antonova E. E., Stepanova M. V., Moya P. S., Pinto V. A., Vovchenko V. V., Ovchinnikov I. L., Sotnikov N. V., 2018, *Earth Planets Space*, 70, 127  
 Aubert H., 1864, *Physiologie der Netzhaut*. Verlag von E. Morgenstern, Breslau (now Wrocław, Poland)  
 Balan N., Tulasiram S., Kamide Y., Batista I. S., Souza J. R., Shiokawa K., Rajesh P. K., Victor N. J., 2017, *Earth Planets Space*, 59, 69  
 Bamba Y., Inoue S., Hayashi K., 2019, *ApJ*, 874, 73  
 Baranyi T., Györi L., Ludmány A., 2016, *Sol. Phys.*, 291, 3081  
 Berrilli F., Giovannelli L., 2022, *J. Space Weather Space Clim.*, 12, 3  
 Blake S., Pulkkinen A., Schuck P., Gloer A., Tóth G., 2021, *JGR Space*, 126, e2020JA028284  
 Boteler D. H., 2019, *Space Weather*, 17, 1427  
 Boué A., 1856, *Akad. Wiss. Wien. Math. Phys.*, C1, 22  
 Carapiperis L. N., 1956, *Pure Appl. Geophys.*, 35, 139  
 Carrington R. C., 1859, *MNRAS*, 20, 13  
 Case N. A., MacDonald E. A., 2015, *Ann. Geophys.*, 56, 3.13  
 Chapanis A., 1947, *J. Gen. Physiol.*, 30, 423  
 Clerke A., 1911, *Encyclopædia Britannica*, 8, 408  
 Cliver E., Dietrich W., 2013, *J. Space Weather Space Clim.*, 3, A31  
 Cliver E., Kamide Y., Ling A., 2002, *J. Atmos. Sol.-Terr. Phys.*, 64, 47  
 Cliver E., Schrijver C., Shibata K., Usoskin I., 2022a, *Living Rev. Sol. Phys.*, 19  
 Cliver E., Pötzi W., Veronig A., 2022b, *ApJ*, 938, 136  
 Cyamukungu M. et al., 2014, *IEEE Trans. Nuclear*, 61, 3667  
 Denton M. H., Borovsky J. E., 2014, *JGR Space Phys.*, 119, 9246  
 Dey A., Zele A. J., Feigl B., Adhikari P., 2021, *Vis. Res.*, 180, 1  
 Dimitrov P., Guymer R., Zele A., Anderson A., Vingrys A., 2008, *Invest. Ophthalm. Vis. Sci.*, 49, 55  
 Emmert J., Richmond A., Drob D., 2010, *JGR Space Phys.*, 115, 2010JA015326  
 Fritz H., 1873, Fritz. H.: *Verzeichnis beobachteter Polarlichter*. C. Gerold's Sohns, Vienna  
 Frobesius J. N., 1739, *Luminis Atque Aurorae Borealis Spectaculorum Recensio Chronologica*. Christian Friedrich Weygandt, Helmstadt, Germany  
 Frost A. M., Owens M. J., Macneil A., Lockwood M., 2022, *Sol. Phys.*, 297, 82:1  
 González-Esparza J. A., Cuevas-Cardona M. C., 2018, *Space Weather*, 16, 593  
 Graham C., Bartlett N., Brown J., Hsia Y., Mueller C., Riggs L., 1965, *Vision and Visual Perception*. Wiley, New York  
 Grandin M. et al., 2024, *EGU sphere*, 2024, 1  
 Green J. L., Boardsen S., 2006, *Adv. Space Res.*, 38, 130  
 Györi L., Ludmány A., Baranyi T., 2017, *MNRAS*, 465, 1259  
 Hapgood M., 2019, *Space Weather*, 17, 950  
 Hayakawa H. et al., 2016, *PASJ*, 68, 99  
 Hayakawa H. et al., 2018a, *ApJ*, 862, 15  
 Hayakawa H., Ebihara Y., Hand D. P., Hayakawa S., Kumar S., Mukherjee S., Veenadhari B., 2018b, *ApJ*, 869, 57  
 Hayakawa H. et al., 2019a, *Space Weather*, 17, 1553  
 Hayakawa H. et al., 2019b, *MNRAS*, 484, 4083  
 Hayakawa H. et al., 2021, *ApJ*, 909, 197  
 Hayakawa H., Nevanlinna H., Blake S. P., Ebihara Y., Bhaskar A. T., Miyoshi Y., 2022, *ApJ*, 928, 32  
 Hayakawa H., Ebihara Y., Hata H., 2023a, *Geosci. Data J.*, 10, 142  
 Hayakawa H., Bechet S., Clette F., Hudson H., Maehara H., Namekata K., Notsu Y., 2023b, *ApJ*, 954, L3  
 Hayakawa H. et al., 2023c, *ApJ*, 959, 23  
 Hayakawa H. et al., 2025, *ApJ*, 979, 49  
 Hecht S., 1920, *J. Gen. Physiol.*, 2, 499  
 Hecht S., Shlaer S., Pirenne M. H., 1942, *J. Gen. Physiol.*, 25, 819  
 Holmes R., 2016, *Phys. World*, 29, 28

- Hudson H., Cliver E., White S., Machol J., Peck C., Tolbert K., Viereck R., Zarro D., 2024, *Sol. Phys.*, 299, 39
- Ishkov V. N., 2016, *Vestn. Otd. nauk Zemle RAN*, 8, 1
- Jackson A., Jonkers A. R. T., Walker M. R., 2000, *Phil. Trans.*, 358, 957
- Jacobsen K. S., Andalsvik Y. L., 2016, *J. Space Weather Space Clim.*, 6, A9
- Kalb V., Kosar B., Collado-Vega Y., Davidson C., 2023, *Earth Space Sci.*, 10, e2022EA002513
- Kalloniatis M., Luu C., 2007, Webvision: The Organization of the Retina and Visual System. University of Utah Health Sciences Center, Salt Lake City, Utah
- Karinen A., Musula K., 2005, *Ann. Geophys.*, 23, 475
- Kataoka R., Nakano S., 2021, *J. Space Weather Space Clim.*, 11, 46
- Kataoka R., Reddy S., Nakano S., Pettit J., Nakamura Y., 2024a, *Sci. Rep.*, 14, 25849
- Kataoka R., Miyoshi Y., Shiokawa K., Nishitani N., Keika K., Amano T., Seki K., 2024b, *Geophys. Res. Lett.*, 51, e2024GL108778
- Kimball D., 1960, A Study of the Aurora of 1859, Geophysical Institute, University of Alaska
- Kistler L. M., 2020, *Geophys. Res. Lett.*, 47, e2020GL090235
- Kletzing C. A., Scudder J. D., Dors E. E., Curto C., 2003, *JGR Space*, 108, 2002JA009678
- Knipp D. J., Bernstein V., Wahl K., Hayakawa H., 2021, *J. Space Weather Space Clim.*, 11, 29
- Kosar B. C., MacDonald E., Case N., Y. Z., Mitchell E. J., Viereck R., 2018, *J. Atmos. Sol.-Terr. Phys.*, 177, 274
- Kozyra J. U., Nagy A. F., Slater D. W., 1997, *Rev. Geophys.*, 35, 155
- Křivský K., Pejml K., 1999, *Publ. Astron. Inst. Czechoslov. Acad. Sci.*, 75, 159
- Kubota Y., Nagatsuma T., Den M., Tanaka T., Fujita S., 2017, *JGR Space*, 122, 4398
- Lang A., 1849, *MNRAS*, 9, 148
- Laundal K. M., Richmond A. D., 2017, *Space Sci. Rev.*, 206, 27
- Lee Y.-S., Kwak Y.-S., Kim K.-C., Solheim B., Lee R., Lee J., 2017, *JGR Space*, 122, 1042
- Liu Z.-Y. et al., 2024, *Geophys. Res. Lett.*, 51, e2023GL107209
- Livesey R. J., 1984, *J. Br. Astron. Assoc.*, 94, 158
- Livesey R. J., 2000, *J. Br. Astron. Assoc.*, 110, 302
- Lockwood M., Barnard L. A., 2015, *Ann. Geophys.*, 56, 4.25
- Lockwood M., Milan S., 2023, *Front. Astron. Space Sci.*, 10, 1139295
- Lockwood M., Owens M. J., 2021, *Ann. Geophys.*, 62, 3.12
- Lockwood M., Owens M., 2024, *Sol. Phys.*, 299, 28
- Lockwood M., Owens M., Rouillard A. P., 2009a, *J. Geophys. Res.: Space Phys.*, 114, A11103
- Lockwood M., Owens M., Rouillard A. P., 2009b, *J. Geophys. Res.: Space Phys.*, 114, A11104
- Lockwood M., Chambodut A., Barnard L. A., Owens M. J., Clarke E., Mendel V., 2018a, *J. Space Weather Space Clim.*, 8, A53
- Lockwood M., Finch I. D., Chambodut A., Barnard L. A., Owens M. J., Clarke E., 2018b, *J. Space Weather Space Clim.*, 8, A58
- Lockwood M., Owens M. J., Barnard L. A., Haines C., Scott C. J., McWilliams K. A., Coxon J. C., 2020a, *J. Space Weather Space Clim.*, 10, 23
- Lockwood M., McWilliams K. A., Owens M. J., Barnard L. A., Watt C. E., Scott C. J., Macneil A. R., Coxon J. C., 2020b, *J. Space Weather Space Clim.*, 10, 30
- Lockwood M., Owens M. J., Barnard L. A., Watt C. E., Scott C. J., Coxon J. C., McWilliams K. A., 2020c, *J. Space Weather Space Clim.*, 10, 61
- Lockwood M., Haines C., Barnard L. A., Owens M. J., Scott C. J., Chambodut A., McWilliams K. A., 2021, *J. Space Weather Space Clim.*, 11, 15
- Lockwood M., Owens M. J., Barnard L. A., Scott C. J., Frost A. M., Yu B., Chi Y., 2022a, *Front. Astron. Space Sci.*, 9, 960775
- Lockwood M., Owens M. J., Yardley S. L., Virtanen I., Yeates A., Muñoz Jaramillo A., 2022b, *Front. Astron. Space Sci.*, 9, 976444
- Lockwood M., Owens M. J., Barnard L. A., 2023, *JGR Space*, 128, e2022JA031177
- Love J., Coisson P., 2016, *Eos*, 97, 18
- Love J. J., Hayakawa H., Cliver E. W., 2019a, *Space Weather*, 17, 1281
- Love J., Hayakawa H., Cliver E., 2019b, *Space Weather*, 17, 1281
- Love J., Rigler E., Hayakawa H., Mursula K., 2024, *J. Space Weather Space Clim.*, 14, 21
- Love J., Mann I., Qvick T., Mursula K., 2025, *Space Weather*, 23, e2024SW004286
- Lovering J., 1868, *Mem. Am. Acad. Arts Sci.*, 10, 55
- Lyman H., 1921, *Mon. Weather Rev.*, 49, 406
- Mairan J. J., 1754, *de Ort, Traite Physique et Historique de l'Aurore Boreale*. Imprimerie Royale, Paris
- Machol J., Viereck R., Peck C., Mothersbaugh J. I., 2022, GOES X-ray Sensor (XRS) Operational Data (v1.5), [https://www.ngdc.noaa.gov/stp/satellite/goes/doc/GOES\\_XRS\\_readme.pdf](https://www.ngdc.noaa.gov/stp/satellite/goes/doc/GOES_XRS_readme.pdf) (Accessed Oct 2024)
- Mandal S., Krivova N., Solanki S., Sinha N., Banerjee D., 2020, *A&A*, 640, A78
- Martinis C., Baumgardner J., Wroten J., Mendillo M., 2018, *Adv. Space Res.*, 61, 1636
- Mathieu E., Rodés-Guirao L., 2022, Our World in Data, available at: <https://ourworldindata.org/population-sources>
- Mayaud P. N., 1980, Derivation, Meaning, and Use of Geomagnetic Indices. Geophysical Monograph Series Vol. 22, American Geophysical Union, Washington, D. C.
- McNish A. G., 1941, *Terr. Mag. Atmos. Elec.*, 46, 461
- Meadows P., 2020, *MNRAS*, 497, 1110
- Meadows P., 2024, *J. Br. Astron. Assoc.*, 134, 215
- Megan Gillies D., Knudsen D., Donovan E., Jackel B., Gillies R., Spanswick E., 2017, *JGR Space*, 122, 8181
- Mikhalev A. V., 2019, *Sol.-Terr. Phys.*, 5, 66
- Mikhalev A., 2024, *Sol.-Terr. Phys.*, 10, 55
- Miyaoka H., Hirasawa T., Yumoto K., Tanaka Y., 1990, *Proc. Japan Acad. B*, 47, 66
- Mursula K., Holappa L., Karinen A., 2011, *J. Atmos. Sol.-Terr. Phys.*, 73, 316
- Nagy A., Roble R., Hays P., 1970, *Space Sci. Rev.*, 11, 709
- O'Brien T. P., McPherron R. L., 2002, *JGR Space*, 107 1341
- Onsager T. G., Lockwood M., 1997, *Space Sci. Rev.*, 80, 77
- Oreshina A. V., Oreshina I. V., Somov B. V., 2012, *A&A*, 538, A138
- Owens M., Lockwood M., Barnard L., 2017a, *Sci. Rep.*, 7, 4152
- Owens M. J., Lockwood M., Riley P., Linker J., 2017b, *JGR Space*, 122, 10980
- Owens M., Lockwood M., Barnard L., Scott C., Haines C., Macneil A., 2021, *Sol. Phys.*, 296, 82
- Peterson B., 2016, Understanding Exposure: How to Shoot Great Photographs with any Camera, 4th edn. AmPhoto Books, Berkeley
- Pictet R., 1872, *Arch. Sci. Phys. Nat.*, 43, 172
- Pierrard V., Lopez Rosson G., 2016, *Ann. Geophys.*, 34, 75
- Pirenne M., 1962, in *The Visual Process*. Elsevier Academic Press, Oxford, p. 93
- Pitsyna N. G., Demina I. M., 2021, *Geomagn. Aeron.*, 61, 312
- Rassoul H. K., Rohrbaugh R. P., Tinsley B. A., 1992, *JGR Space*, 97, 4041
- Reed E., Blamont J., 1974, *J. Geophys. Res.*, 79, 2524
- Rees M., 1969, *Space Sci. Rev.*, 10, 413
- Richmond A. D., 1995, *J. Geomagn. Geoelectr.*, 47, 191
- Russell C. T., McPherron R. L., 1973, *J. Geophys. Res.*, 78, 92
- Sergeev V., Bondareva T., Gilles D., Donovan E., 2020, *J. Atmos. Sol.-Terr. Phys.*, 204, 105288
- Seydl A., 1954, *Geofys. S.*, 17, 159
- Shao X., Cao C., Liu T.-C., Zhang B., Fung S. F., Sharma A., 2016, *IGARSS*, 2016, 3021
- Shepherd S. G., 2014, *JGR Space*, 119, 7501
- Shiokawa K., Yumoto K., Tanaka Y., Oguti T., Kiyama Y., 1994, *J. Geomagn. Geoelectr.*, 46, 231
- Shiokawa K., Yumoto K., Meng C.-I., Reeves G., 1996, *Geophys. Res. Lett.*, 23, 2529
- Shiokawa K., Ogawa T., Kamide Y., 2005, *JGR Space Phys.*, 110, 2004JA010706
- Shiokawa K., Miyoshi Y., Brandt P. C., Evans D. S., Frey H. U., Goldstein J., Yumoto K., 2013, *JGR Space*, 118, 256
- Silverman S. M., 1992, *Rev. Geophys.*, 30, 333
- Silverman S., 1995, *J. Atmos. Terr. Phys.*, 57, 673

- Silverman S., 1998, *J. Atmos. and Sol.-Terr. Phys.*, 60, 997
- Silverman S., 2006, *Adv. Space Res.*, 38, 136
- Silverman S., 2008, *J. Atmos. Sol.-Terr. Phys.*, 70, 1301
- Silverman S., Cliver E., 2001, *J. Atmos. Sol.-Terr. Phys.*, 63, 523
- Silverman S. M., Hayakawa H., 2021, *J. Space Weather Space Clim.*, 11, 17
- Siscoe G., Crooker N., Clauer C., 2006, *Adv. Space Res.*, 38, 173
- Srivastava N., Mathew S., Louis R., Wiegmann T., 2009, *JGR Space*, 114, 2008JA013845
- Sterken C., Stauber K. B., 2000, *J. Astron. Data*, 6, 7
- Thomson G. H., 2005, *Imaging Sci. J.*, 53, 226
- Tinsley B. A. et al., 1984, *Geophys. Res. Lett.*, 11, 572
- Tinsley B. A., Rohrbaugh R., Rassoul H., Sahai Y., Teixeira N. R., Slater D., 1986, *JGR Space*, 91, 11257
- Tredici T., Miller R., 1985, Technical Report 83–3, ADA159720, Night Vision Manual for the Flight Surgeon, Armstrong Laboratory, Human Systems Center (AFMC), Brooks Air Force Base, Texas, available at: <https://apps.dtic.mil/sti/tr/pdf/ADA159720.pdf>
- Valach F., Hejda P., Revallo M., Bochníček J., 2019, *J. Space Weather Space Clim.*, 9, A11
- van der Meeren C., Laundal K., Burrell A., Lamarche L., Starr G., Reimer A., Morschhauser A., 2023, *aburrell/apexpy: ApexPy Version 2.0.1*, Zenodo
- Vaquero J. M., Valente M. A., Trigo R. M., Ribeiro P., Gallego M. C., 2008, *JGR Space*, 113, 2007JA012943
- Vasil'ev V. N., Tibilov A. S., 2018, *J. Optic. Tech.*, 85, 157
- Vázquez M., Vaquero J. M., 2010, *Sol. Phys.*, 267, 431
- Vázquez M., Vaquero J. M., Gallego M. C., Roca Cortés T., Pallé P. L., 2016, *Sol. Phys.*, 291, 613
- Vichare G., Bhaskar A., Rawat R., Yadav V., Mishra W., Angchuk D., Singh A. K., 2024, *ApJ*, 977, 171
- Welling D. T. et al., 2015, *Space Sci. Rev.*, 192, 145
- Willis D. M., Henwood R., Stephenson F. R., 2006, *Ann. Geophys.*, 24, 2743
- Willis D. M., Henwood R., Stephenson F. R., 2009, *Ann. Geophys.*, 27, 185
- Wolf R., 1857, *Vier. Nat. Ges.in Zürich*, 2, 253
- Wu C.-C., Liou K., Lepping R. P., Huttig L., Plunkett S., Howard R. A., Socker D., 2016, *Earth Planets Space*, 68, 151
- Yokoyama N., Kamide Y., Miyaoka H., 1998, *Ann. Geophys.*, 16, 566
- Zhang Q.-H., Lockwood M., Foster J. C., Zong Q., Dunlop M. W., Zhang S., Moen J. I., Zhang B., 2018, *Sci. Bul.*, 63, 31
- Zhao H., Zong Q.-G., 2012, *JGR Space*, 117, A11222
- Zöllner F., 1870, *Ann. Phys.*, 217, 574

## SUPPORTING INFORMATION

Supplementary data are available at *MNRAS* online.

Please note: Oxford University Press is not responsible for the content or functionality of any supporting materials supplied by the authors. Any queries (other than missing material) should be directed to the corresponding author for the article.

This paper has been typeset from a  $\text{\LaTeX}$  file prepared by the author.